

1 A daily highest air temperature estimation method and
2 spatial-temporal changes analysis of high temperature in
3 China from 1979 to 2018

4 Ping Wang^{1,2*}, Kebiao Mao^{1,3*}, Fei Meng², Zhihao Qin³, Shu Fang⁴, Sayed M. Bateni⁵,
5 Mansour Almazroui^{6,7}

6 ¹ School of Physics and Electronic-Engineering, Ningxia University, Yinchuan 750021, China

7 ² School of Surveying and Geo-Informatics, Shandong Jianzhu University, Jinan 250100, China

8 ³ Institute of agricultural resources and regional planning, Chinese Academy of Agricultural
9 Sciences, Beijing 100081, China

10 ⁴ School of Earth Sciences and Resources, China University of Geosciences, Beijing 100083, China

11 ⁵ Department of Civil and Environmental Engineering and Water Resources Research Center,
12 University of Hawaii at Manoa, Honolulu, HI 96822, USA

13 ⁶ Centre of Excellence for Climate Change Research/Department of Meteorology, King Abdulaziz
14 University, Jeddah 21589, Saudi Arabia

15 ⁷ Climatic Research Unit, School of Environmental Sciences, University of East Anglia, Norwich,
16 UK

17 Correspondence to: Kebiao Mao (maokebiao@caas.cn)

18 ★ These authors contributed equally to this works.

19 **Abstract.** The daily highest air temperature (T_{\max}) is a key parameter for global and regional high
20 temperature analysis, which is very difficult to be obtained in areas where there are no
21 meteorological observation stations. This study proposes an estimation framework for obtaining
22 high-precision T_{\max} . Firstly, we build a near surface air temperature diurnal variation model to
23 estimate T_{\max} for China from 1979 to 2018 based on multi-source data. Then in order to further
24 improve the estimation accuracy, we divided China into six regions according to climate conditions
25 and topography, and established calibration models for different ~~region~~regions. The analysis shows
26 that the mean absolute error (MAE) of the dataset (<https://doi.org/10.5281/zenodo.56028976322881>)
27 is about 1.07 °C and RMSE is 1.52 °C, which improves the accuracy of the traditional method by
28 nearly 1 °C. The spatial-temporal variations analysis of T_{\max} in China indicated that the annual and
29 seasonal mean T_{\max} in most areas of China showed an increasing trend. In summer and autumn, the

30 T_{\max} in northeast China increased the fastest among the six regions, which were $0.4^{\circ}\text{C}/10\text{a}$ and
31 $0.39^{\circ}\text{C}/10\text{a}$, respectively. The number of summer days and warm days showed an increasing trend
32 in all regions, while the number of icing days and cold days showed a decreasing trend. The
33 abnormal temperature changes mainly occurred in El Niño years or La Niña years. We found that
34 the influence of the Indian Ocean Basin Warming (IOBW) on air temperature in China were
35 generally greater than those of the North Atlantic Oscillation and the NINO3.4 area sea surface
36 temperature after making analysis of ocean climate modal indices with air temperature. In general,
37 this T_{\max} dataset and analysis are of great significance to the study of climate change in China,
38 especially for environmental protection.

39 **Keywords:** Near surface air temperature diurnal variation model; Daily highest air temperature; High temperature;
40 Spatial-temporal analysis; Climate change

41 **1 Introduction**

42 In the context of global warming, the frequency of high temperature events is increasing, and high
43 temperature tends to increase electricity demand and energy consumption (Zhang et al., 2021;
44 Sathaye et al., 2013), adversely affecting human health, social economy and ecosystem (Sehra et al.,
45 2020; Basu, 2009; Gasparrini and Armstrong, 2011). The daily highest air temperature (T_{\max}) is the
46 basic parameter for studying regional scale high-temperature events. It has a great influence on the
47 ozone concentration (Abdullah et al., 2017; Kleinert et al., 2021) and the start time of the plant
48 growth season [on the Tibetan Plateau](#) (Yang et al., 2017). T_{\max} is not only an important factor for
49 high temperature disaster risk assessment, but also a key input parameter for crop growth models
50 and carbon emission ~~model~~ [models](#). Sustained and abnormally high T_{\max} will cause high temperature
51 heat damage and adversely affect crop growth. Therefore, it is very important to accurately obtain

52 the temporal and spatial distribution of T_{\max} and study the characteristics of high temperature
53 weather. Generally, T_{\max} is measured on a thermometer in a louvered box 1.5 meters above the
54 ground in the field. Although the T_{\max} measured by this method has high accuracy but not spatial
55 continuity. Therefore, some scholars ~~spatializes~~spatialized the station based T_{\max} through methods
56 such as Kriging interpolation and spline function interpolation. However, the number of
57 meteorological stations is limited, and stations in remote areas and areas with complex terrain are
58 even sparser, which makes the accuracy of T_{\max} obtained by interpolation difficult to meet the
59 requirements of regional scale research in China.

60 In order to obtain information about the spatial distribution of the T_{\max} , many scholars began to
61 use satellite remote sensing to solve this problem. There are three commonly remote sensing
62 methods to estimate T_{\max} . The first method is regression analysis, which uses the correlation
63 between retrieved land surface temperature (LST) and T_{\max} to establish a regression model to
64 estimate T_{\max} (Shen and Leptoukh, 2011; Evrendilek et al., 2012; Lin et al., 2012). The second
65 method is machine learning, which can flexibly estimate T_{\max} in urban areas with complex features
66 (Yoo et al., 2018). The third method is to use a diurnal temperature change model to extend the
67 instantaneous air temperature (T_a) to calculate T_{\max} , either by the Temperature-Vegetation Index
68 (TVX) method (Wloczyk et al., 2011; Zhu et al., 2013), the energy balance method (Sun et al., 2005;
69 Zhu et al., 2017), the atmospheric temperature profile extrapolation method (Fabiola and Mario,
70 2010), or other methods. The above methods of estimating T_{\max} with LST can better reflect the
71 spatial distribution of T_{\max} , but regression analysis and machine learning require sufficient and
72 representative samples, and the established model is not universal. TVX cannot estimate T_a at night
73 and in sparse vegetation areas. Many parameters required by the energy balance method cannot

74 usually be obtained by remote sensing technology. The estimation accuracy of atmospheric
75 temperature profile extrapolation method is greatly affected by the accuracy of the atmospheric
76 temperature profile. Therefore, a new method for estimating T_{\max} needs to be proposed.

77 At present, most researches mainly used the extreme climate indices defined by the Expert
78 Team on Climate Change Detection and Indices (ETCCDI) to analyze the temporal and spatial
79 distribution characteristics of high temperature and its changing laws (Khan et al., 2018; Mcgree
80 et al., 2019; Poudel et al., 2020; Ruml et al., 2017; Salman et al., 2017; Wang et al., 2019; Zhang
81 et al., 2019). Zhou et al. (2016) analyzed the temperature indices changes in China from 1961 to 2010,
82 and the results indicated that the warm extremes in China exhibited an increasing trend. In addition,
83 the researchers analyzed the characteristics of high temperature changes in the Three River
84 Headwaters, Yangtze River Basin, Loess Plateau, Inner Mongolia and Songhua River Basin (Ding
85 et al., 2018; Guan et al., 2015; Sun et al., 2016; Tong et al., 2019; Zhong et al., 2017). In addition
86 to analyzing the temporal and spatial changes of high temperature events, many scholars have also
87 studied the influencing factors of high temperature events. Studies showed that extreme high
88 temperature over China was related to abnormal atmospheric circulation disturbances (You et al.,
89 2011; Zhong et al., 2017) and abnormal sea surface temperature (Li et al., 2019b; Wu et al., 2011).
90 However, previous studies on the cause of high temperature events usually only analyzed the
91 correlation between atmospheric circulation modes and the temperature indices along the time
92 dimension, without considering the spatial characteristics of the correlation.

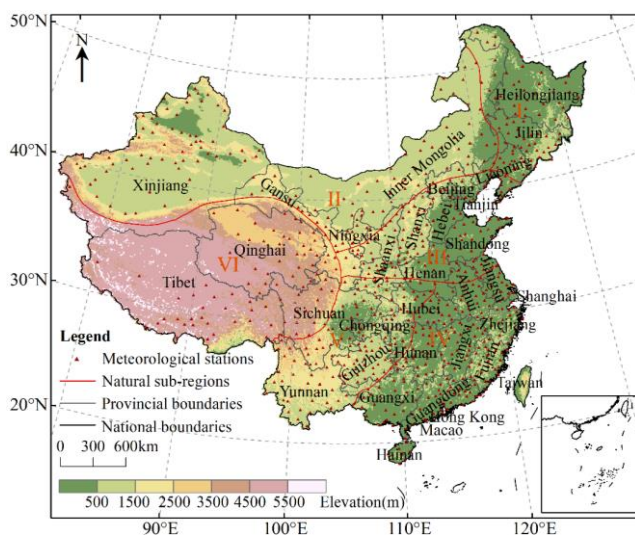
93 From the above analysis, most of the researches mainly ~~use~~used the meteorological observation
94 temperature data interpolation to analyze local temperature changes, and ~~almost as far as we know,~~
95 no one ~~constructs~~constructed continuous high-temporal resolution T_{\max} for high temperature

96 analysis in China. In order to better study regional high temperature events, this study proposes an
97 estimation framework for obtaining high-precision T_{\max} . Firstly, we used multi-source data and
98 established near surface T_a diurnal variation model to build T_{\max} dataset in China from 1979 to 2018.
99 To further improve the accuracy, we divided China into six regions according to climate conditions
100 and topography, and established calibration models respectively. On this basis, we further analyzed
101 the spatial-temporal variation characteristics of T_{\max} and corresponding influencing factors in China.
102 This can provide evidence for mitigating global climate change and reducing regional carbon
103 emissions for environmental protection.

104 2 Study area

105 In order to establish a more high-precision T_{\max} dataset to analyze the temporal and spatial
106 characteristics of high-temperature in China, we divided ~~the country~~China into six regions mainly
107 based on topographic conditions (elevation), and climatic conditions, (T_a and precipitation), as
108 shown in Fig.1. (I) The northeast region has a temperate monsoon climate. Affected by the monsoon,
109 ~~T_a is higher in winter~~ in the southern part of the region, ~~but it is the opposite~~higher than that in the
110 ~~northern part~~north in winter. The topography of this area is dominated by plains, hills, and
111 mountains. Due to the influence of topography, the variability of T_a is large in local areas. (II) The
112 northwestern region is dominated by a temperate continental climate (cold in winter and hot in
113 summer) with a large annual and daily T_a range. The area ~~is with~~exhibits little annual precipitation
114 ~~decreasing~~which decreases from east to west. The topography of this area is dominated by plateau
115 basins and rivers are scarce. (III) North China is located in a semi-humid and humid zone in the
116 warm temperate zone. Precipitation is mainly concentrated in summer. This area is dominated by
117 plains and plateaus, bounded by Taihang Mountain, the Loess Plateau in the west, and the North

118 China Plain in the east. (IV) The southeast region is dominated by mountains and hills, which
 119 belongs to the warm and humid subtropical oceanic monsoon climate zone, and the tropical
 120 monsoon climate zone. The climate is mild, with an annual average T_a of 17-21°C and an average
 121 rainfall of 1400-2000mm. (V) The southwestern region has a subtropical monsoon climate, affected
 122 by the southeast monsoon and southwest monsoon. It is hot and rainy in summers, and the landforms
 123 in this area are dominated by plateaus and mountains. (VI) The Qinghai-Tibet Plateau is located in
 124 southwest China, with an average elevation of more than 4,000 meters. The towering terrain has a
 125 great impact on the climate in eastern and southwestern China. It has a plateau mountainous climate,
 126 with cold winters and warm summers, with aridity and little rain throughout the year.



127
 128 **Figure 1.** Overview of the study area.

129 **3 Data**

130 **3.1 China Meteorological Forcing Dataset (CMFD)**

131 CMFD is developed by the Hydro-meteorological Research Group of the Institute of Tibetan Plateau
 132 Research, Chinese Academy of Sciences. The dataset can be obtained from the National Qinghai-

133 Tibet Plateau Science Data Center (<https://data.tpc.ac.cn/>). The near surface T_a data of CMFD has
134 a time resolution of 3h and a spatial resolution of 0.1° , and its accuracy in China is better than Global
135 Land Data Assimilation System (GLDAS) data (He et al., 2020); [CMFD data used ANUSPLIN](#)
136 [software to interpolate the difference between GLDAS \$T_a\$ data and the measured \$T_a\$ data to obtain](#)
137 [grid data, and then the difference grid data and the spatially downscaled GLDAS \$T_a\$ data were](#)
138 [spatially added to generate high resolution \$T_a\$ data](#). The T_a data of CMFD have been widely used in
139 climate simulation, hydrological simulation, vegetation greenness research, and cross-validation of
140 new T_a datasets (Luan et al., 2020; Gu et al., 2020; Wang et al., 2020). Although this dataset has
141 become one of the most widely used climate datasets in China, it does not provide the T_{max} value.
142 In order to perform high temperature analysis, we need to construct a T_{max} dataset.

143 3.2 ERA5 data

144 ERA5 data is the fifth generation of global climate reanalysis data produced by the European Centre
145 for Medium-range Weather Forecast (ECMWF) after ERA-Interim. The model version used by
146 ERA5 is IFS Cycle 41r2, and its spatial-temporal resolution and number of vertical layers are much
147 higher than the ERA-Interim data (Hoffmann et al., 2019; Urraca et al., 2018); [Hersbach et al.,](#)
148 [2020](#)). ERA5 reanalysis data provide a variety of meteorological elements, including atmospheric
149 parameters, land parameters, and ocean parameters, spanning a time range from 1950 to present.
150 The data can be obtained from ~~the ECMWF ERA5 data website~~ [Copernicus Climate Data Store](#)
151 (<https://cds.climate.copernicus.eu/>). The ERA5 dataset also does not provide the T_{max} . This study
152 used T_a data from 1979 to 2018 [with a time resolution of 1 h and a spatial resolution of \$0.25^\circ\$](#) to help
153 build a T_{max} estimation model to generate T_{max} value, [and we have performed multiple kinds of data](#)
154 [assimilation](#).

155 3.3 Meteorological station data

156 T_{\max} data from the China Surface Climatic Data Daily Dataset (V3.0) from 1979 to 2018 were used
157 to verify the accuracy of T_{\max} estimations. The hourly T_a observation data from China
158 meteorological stations were used to determine the occurrence times of T_{\max} and daily lowest air
159 temperature (T_{\min}). Both datasets are from CMA National Meteorological Information Center
160 (<http://data.cma.cn/>). The data were subjected to preliminary quality control and evaluation by CMA,
161 and all elements in the observational data are of high quality and completeness, with the validity
162 rate generally above 99%. These datasets have been widely used in Chinese climate research (Li et
163 al., 2019a; Tong et al., 2019). To ensure the validity of the site data, manual checks were performed
164 on all observed data, including extreme value tests and spatial-temporal consistency tests, and
165 continuous missing data due to instrument damage and other reasons were eliminated. There are
166 824 stations for T_{\max} observation data and 2633 stations for hourly T_a observation data. After
167 performing checks and tests, we used T_{\max} data from 760 meteorological ground stations and hourly
168 T_a data from 2421 meteorological ground stations.

169 3.4 Ocean climate modal indices

170 The ocean occupies about 71% of the earth's surface area, which has a great impact on climate
171 change. After considering the distribution characteristics of China's land and sea, we analyzed the
172 effects of the following ocean climate modal indices on high temperature in China: Indian Ocean
173 Basin warming (IOBW) index, North Atlantic Oscillation (NAO) index, and NINO3.4 area sea
174 surface temperature (NINO3.4) index. Among them, the IOBW index comes from the National
175 Climate Center of CMA (<http://cmdp.ncc-cma.net/cn/index.htm>), and the NAO index and NINO3.4
176 index are from the National Oceanic and Atmospheric Administration of the United States

177 (<https://psl.noaa.gov/data/climateindices/list/>). The time range of the three indices is 1979-2018, and
178 the time scale is monthly.

179 **4 Methodology**

180 4.1 T_{\max} dataset construction

181 At present, the data used in the research on high temperature characteristics is mostly meteorological
182 station data, or grid data obtained by interpolation of station data. A limited number of stations
183 cannot represent the high temperature distribution at large scale. For regions where the stations are
184 very sparse, grid data obtained by spatial interpolation can hardly meet the accuracy requirements
185 of high temperature feature analysis. Although LST can be used to estimate T_{\max} , LST has degraded
186 value in the presence of clouds or rainfall. Therefore, in order to obtain a T_{\max} dataset with high
187 temporal and spatial resolution, we propose a T_{\max} construction model that combines meteorological
188 station data and reanalysis data, and [consider](#) the T_{\max} construction under clear sky and
189 non-clear sky conditions ([see Section 4.1.1 for details](#)). The data processing process is shown in
190 Fig. 2, and the data construction model is divided into two steps: T_{\max} estimation and T_{\max} correction.
191 First, the occurrence time of T_{\max} and T_{\min} was determined pixel by pixel ([see Section 4.1.1 for](#)
192 [details](#)). Then, T_{\max} was determined according to the weather state. (1) In clear sky conditions,
193 CMFD 3h near-surface T_a data was used to construct the T_a diurnal variation model which in turn
194 yielded T_{\max} . (2) In non-clear sky conditions, the site and reanalysis data were used to fill pixels.
195 Finally, the correction model was used to correct the poor quality pixels to generate the final T_{\max}
196 dataset in China.

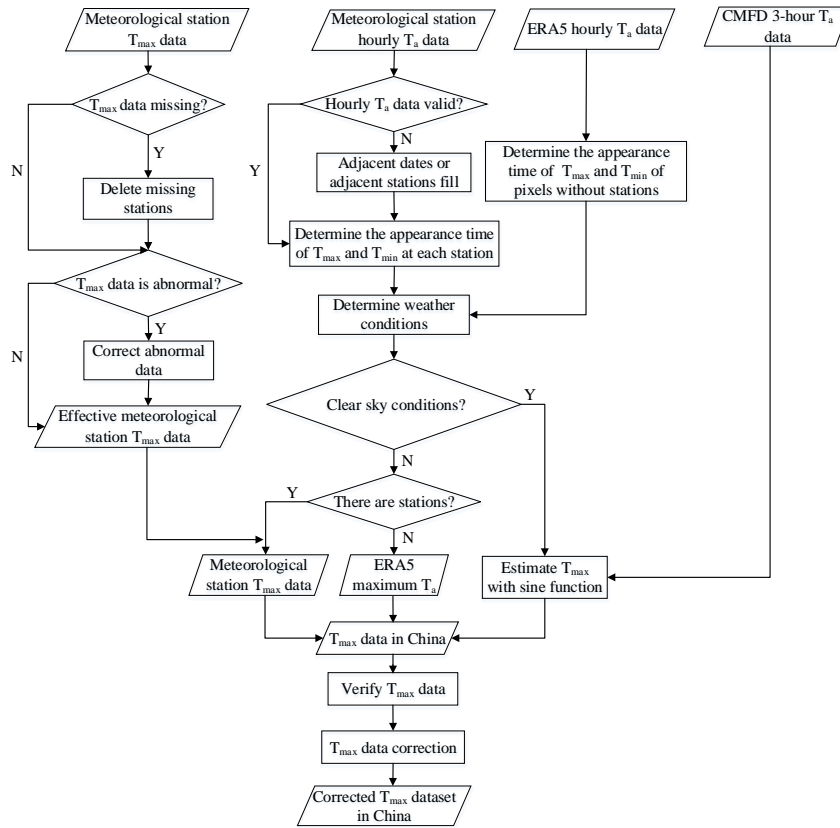


Figure 2. Technical roadmap for T_{\max} estimation.

197

198

199 4.1.1 T_{\max} estimation

200 The changes of T_a under different weather conditions are different. The changes of T_a under clear

201 sky conditions are relatively smooth and regular. Under non-clear sky conditions, T_a changes more

202 drastically. In order to improve the accuracy of T_{\max} estimation, we determined the occurrence time

203 of T_{\max} and T_{\min} pixel by pixel. If there was a meteorological station at the pixel location, the analysis

204 could be divided into two situations. (1) If hourly T_a data was valid, it was directly used to determine

205 the occurrence time of T_{\max} and T_{\min} . (2) If there was a missing value in the hourly T_a data at a

206 certain time, then we used the valid data from adjacent stations at the same time or adjacent time at

207 the same stations to fill in the missing point values. At present, there are not many meteorological

208 stations in China, and the pixels without stations account for 97.5%. If there was no meteorological

209 station at the pixel location, we used ERA5 hourly T_a data to determine the occurrence time of T_{\max}

210 and T_{\min} . [Since the spatial resolution of the ERA5 data is lower than that of the dataset we produce,](#)
 211 [in order to match the two data spatially, we sample the two data to the same resolution, and then use](#)
 212 [latitude and longitude as control conditions to match the different data.](#)

213 Studies have shown that the change of T_a under clear sky conditions follows a certain law: the
 214 change curve of T_a during the day is close to a sine function (Ephraim et al., 1996; Johnson and
 215 Fitzpatrick, 1977; Parton and Logan, 1981; Zhu et al., 2013), so we used [sine function](#) to simulate
 216 the change of T_a during the day. The appearance time of T_{\min} is t_{\min} , and the appearance time of
 217 T_{\max} is t_{\max} . According to the periodicity of the sine function, the model of the change of T_a during
 218 the day is obtained like Eq. (1).

$$219 \quad T_a(t) = A \sin\left(\frac{\pi(t-t_{\min})}{t_{\max}-t_{\min}} - \frac{\pi}{2}\right) + B \quad (1)$$

$$220 \quad \begin{cases} \frac{\partial \delta}{\partial A} = \sum_{i=1}^n \left\{ 2 * \sin\left(\frac{\pi(t_i-t_{\min})}{t_{\max}-t_{\min}} - \frac{\pi}{2}\right) * \left[A * \sin\left(\frac{\pi(t_i-t_{\min})}{t_{\max}-t_{\min}} - \frac{\pi}{2}\right) + B - T_{ai} \right] \right\} = 0 \\ \frac{\partial \delta}{\partial B} = \sum_{i=1}^n \left\{ 2 * \left[A * \sin\left(\frac{\pi(t_i-t_{\min})}{t_{\max}-t_{\min}} - \frac{\pi}{2}\right) + B - T_{ai} \right] \right\} = 0 \\ \delta = \sum_{i=1}^n \left[A * \sin\left(\frac{\pi(t_i-t_{\min})}{t_{\max}-t_{\min}} - \frac{\pi}{2}\right) + B - T_{ai} \right]^2 \end{cases} \quad (2)$$

$$221 \quad \begin{cases} \frac{\partial \delta}{\partial A} = \sum_{i=1}^n \left\{ 2 * \sin\left(\frac{\pi(t_i-t_{\min})}{t_{\max}-t_{\min}} - \frac{\pi}{2}\right) * \left[A * \sin\left(\frac{\pi(t_i-t_{\min})}{t_{\max}-t_{\min}} - \frac{\pi}{2}\right) + B - T_{ai} \right] \right\} = 0 \\ \frac{\partial \delta}{\partial B} = \sum_{i=1}^n \left\{ 2 * \left[A * \sin\left(\frac{\pi(t_i-t_{\min})}{t_{\max}-t_{\min}} - \frac{\pi}{2}\right) + B - T_{ai} \right] \right\} = 0 \\ \delta = \sum_{i=1}^n \left[A * \sin\left(\frac{\pi(t_i-t_{\min})}{t_{\max}-t_{\min}} - \frac{\pi}{2}\right) + B - T_{ai} \right]^2 \end{cases} \quad (2)$$

222 Here n is the number of CMFD near surface T_a data used to construct the T_a change model in a
 223 day. CMFD can obtain T_a data 8 times a day. This study uses four daytime T_a data to construct a T_a
 224 variation model, so n is 4. T_{ai} is the near surface T_a data at the i th time of CMFD, and δ is the sum
 225 of squares of the difference between the model estimated T_a and the near surface T_a of the CMFD.
 226

227 Since the change of T_a under non-clear sky conditions does not conform to the sine curve change,
 228 we divided the estimation of T_{\max} under non-clear sky conditions into two situations. (1) If there
 229 was a station at the location of the pixel, the measured T_{\max} at the station was directly used as the
 230 T_{\max} of the pixel. (2) If there was no measured T_{\max} at the pixel location, the highest value of hourly
 231 T_a of ERA5 in a day was taken as T_{\max} . [Then \$T_{\max}\$ determined by the ERA5 data was assigned to](#)
 232 [the pixel at the corresponding position of the \$T_{\max}\$ image we established using the spatial matching](#)
 233 [method.](#)

234 4.1.2 T_{\max} correction

235 The validation of T_{\max} showed some differences between the estimated T_{\max} and the measured T_{\max} .
 236 In order to further improve the accuracy of T_{\max} , the measurements taken at weather stations should
 237 be used to correct the estimated T_{\max} , as shown in Fig. 3. [First, determine whether there is station](#)
 238 [data at the pixel location. For pixels with stations, it is further judged whether the estimated \$T_{\max}\$ is](#)
 239 [valid by comparing the measured \$T_{\max}\$ with the estimated \$T_{\max}\$.](#) For a pixel with poor quality, if there
 240 is station data at the location of the pixel, the low-quality pixel will be replaced with the measured
 241 data from the station. If there is no station data at the pixel location, the data is corrected by multiple
 242 linear regression method (Ninyerola et al., 2000; Zhao et al., 2020; Zheng et al., 2013). By
 243 establishing the regression relationship between station T_{\max} and estimated T_{\max} , the residuals were
 244 calculated according to the measured values and T_{\max} regression predicted values, and the spatial
 245 distribution of the residuals was obtained by the inverse distance weight (IDW) interpolation method.
 246 Finally, the estimated T_{\max} and the residual were added to obtain the corrected T_{\max} . The calibration
 247 model is like Eq. (3) and Eq. (4).

$$248 \quad T_{after}(i,j) = T_{before}(i,j) + \hat{\epsilon}(i,j) \quad (3)$$

$$249 \quad \hat{\epsilon}(i,j) = T_{true}(i,j) - T_{forecast}(i,j) \quad (4)$$

250 Here i and j are the row and column numbers of the image, $T_{after}(i,j)$ is T_{\max} after correction,
 251 $T_{before}(i,j)$ is T_{\max} before correction, $\hat{\epsilon}(i,j)$ is the residual, $T_{true}(i,j)$ is the measured T_{\max} , and
 252 $T_{forecast}(i,j)$ is T_{\max} predicted by the regression model.

253 We used the jackknife method to randomly divide the station data into calibration and
 254 verification data (Benali et al., 2012; Zhao et al., 2020). We selected 80% of the meteorological
 255 stations to establish the regression relationship between the measured and estimated T_{\max} values.
 256 The other 20% of the meteorological stations were used to verify the accuracy of the corrected data.
 257 In order to improve data accuracy, the dataset used in the subsequent analysis of spatial-temporal
 258 variation of high temperature was the data corrected by all stations. Due to the different topographic
 259 and climatic characteristics of the six natural regions, the linear models of estimated T_{\max} and
 260 measured T_{\max} in each region were different. In order to obtain a higher-precision correction, the six
 261 regions were corrected separately.

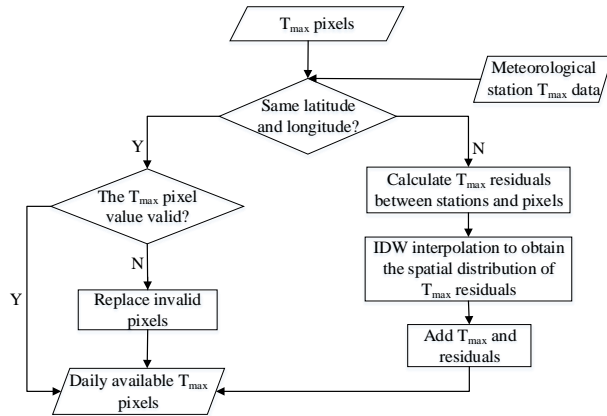


Figure 3. Flow chart of T_{\max} correction.

4.2 Extreme temperature indices

ETCCDI proposed a set of extreme climate indices in the Climate Change Monitoring conference, which became the unified standard for climate change research (Hong and Ying, 2018; Mcgree et al., 2019; Poudel et al., 2020; Zhang et al., 2019; Zhou et al., 2016). Among them, 27 indices are considered as core indices, which are calculated from daily T_a and precipitation data and have the characteristics of weak extremeness, low noise, and strong significance. These indices comprehensively capture the frequency, intensity and duration of extreme climate events, and are recommended as the core indicators for extreme climate event analysis by the STARDEX program of the European Union (Guan et al., 2015; Ruml et al., 2017). In this study, six temperature indices related to T_{\max} were used to analyze high temperature characteristics, and their definitions are shown in Table 1. Among them, the 90th percentile in TX90p and the 10th percentile in TX10p were obtained in ascending order based on the T_{\max} data of each month during 1979-2018.

Table 1. Definition of extreme temperature indices.

Index	Name	Definition	Category	Unit
SU	Summer days	Annual count of days when $T_{\max} > 25^{\circ}\text{C}$	Frequency	d
TX90p	Warm days	Annual count of days when $T_{\max} > 90\text{th percentile}$	Frequency	d
TXn	Minimum T_{\max}	Annual minimum value of T_{\max}	Intensity	$^{\circ}\text{C}$

设置了格式: 字体: 加粗

域代码已更改

域代码已更改

<u>TXx</u>	<u>Maximum T_{max}</u>	<u>Annual maximum value of T_{max}</u>	<u>Intensity</u>	<u>°C</u>
<u>ID</u>	<u>Icing days</u>	<u>Annual count of days when T_{max} < 0°C</u>	<u>Frequency</u>	<u>d</u>
<u>TX10p</u>	<u>Cold days</u>	<u>Annual count of days when T_{max} < 10th percentile</u>	<u>Frequency</u>	<u>d</u>

277 4.3 Trend analysis

278 4.3.1 Sen's slope estimation

279 In this study, the trends of T_{max} and extreme temperature indices were calculated using Sen's slope
 280 estimation. Sen's slope estimation is a nonparametric estimation method. Even if there are some
 281 outliers in the sample, it can reliably estimate the change trend of the time series, so it is widely used
 282 in trend analysis (Sen, 1968; Zhang et al., 2017). The Eq. (5) is used to calculate the slope of each
 283 pair of data.

$$284 K_i = \frac{x_k - x_j}{k - j} \quad (i = 1, 2, \dots, N) \quad (5)$$

285 Where $N = \frac{n(n-1)}{2}$, x_k and x_j are the time series values of the k th and j th samples respectively
 286 ($1 \leq j < k \leq n$). Arranging the N , K_i values in ascending order, the median Sen's slope is
 287 estimated as Eq. (6).

$$288 \text{Slope} = \begin{cases} K_{[(N+1)/2]} & , N \text{ is odd} \\ \frac{K_{[N/2]} + K_{[(N+2)/2]}}{2} & , N \text{ is even} \end{cases} \quad (6)$$

289 4.3.2 Mann-Kendall trend test

290 Mann-Kendall trend test is used to test the trends of T_{max} and extreme temperature indices. Mann-
 291 Kendall method does not require samples to follow a certain distribution and is not disturbed by a
 292 few outliers, and it can test the change trend of time series (Seenu and Jayakumar, 2021; Tan et al.,
 293 2019). Eq. (7) is used to calculate the statistic of the Mann-Kendall trend test.

$$294 S = \sum_{i=1}^{n-1} \sum_{j=i+1}^n \text{sgn}(x_j - x_i) \quad (7)$$

$$295 \text{sgn}(x_j - x_i) = \begin{cases} 1 & , x_j - x_i > 0 \\ 0 & , x_j - x_i = 0 \\ -1 & , x_j - x_i < 0 \end{cases} \quad (8)$$

$$296 \text{Var}(S) = \frac{n(n-1)(2n+5)}{18} \quad (9)$$

297 Here x_i and x_j are the i th and j th data values of the time series, and n is the length of the time
 298 series, where n is 40. $\text{Var}(S)$ is the variance of S . The standardized statistic Z_c is computed by using
 299 Eq. (10).

$$300 \quad Z_c = \begin{cases} \frac{S-1}{\sqrt{\text{Var}(S)}}, & S > 0 \\ 0, & S = 0 \\ \frac{S+1}{\sqrt{\text{Var}(S)}}, & S < 0 \end{cases} \quad (10)$$

301 When $|Z_c| > Z_{1-\alpha/2}$, the change trend is considered to be significant. Here, $Z_{1-\alpha/2}$ is the
 302 standard normal variance, α is the significance test level, when $\alpha = 0.05$, $Z_{1-\alpha/2} = 1.96$, and
 303 when $\alpha = 0.01$, $Z_{1-\alpha/2} = 2.58$.

304 4.4 Mann-Kendall test for abrupt change analysis

305 Climate system change is an unstable and discontinuous change process, and one of the commonly
 306 used methods to test its change is the Mann-Kendall mutation test, which is very effective in testing
 307 the change of elements from a relatively stable state to another state (Ruml et al., 2017). [We used](#)
 308 [Mann-Kendall mutation test to test whether extreme temperature indices has mutation](#). For a time
 309 series x with n samples, Eq. (11) is used to construct an ordered sequence.

$$310 \quad s_k = \sum_{i=1}^k r_i \quad (k = 2, 3, \dots, n) \quad (11)$$

$$311 \quad r_i = \begin{cases} +1, & x_i > x_j \\ 0, & x_i \leq x_j \end{cases} \quad (j = 1, 2, \dots, i) \quad (12)$$

$$312 \quad UF_k = \frac{s_k - E(s_k)}{\sqrt{\text{Var}(s_k)}} \quad (k = 1, 2, \dots, n) \quad (13)$$

$$313 \quad E(s_k) = \frac{k(k-1)}{4} \quad (14)$$

$$314 \quad \text{Var}(s_k) = \frac{k(k-1)(2k+5)}{72} \quad (15)$$

315 Where s_k is the cumulative count of the number of values at time i greater than that at time j .
 316 $E(s_k)$ and $\text{Var}(s_k)$ are the mean and variance of the cumulative number s_k respectively. UF_k is a
 317 standard normal distribution, given the significance level α , and [may can](#) be obtained from the
 318 normal distribution table. If $|UF_k| > U_\alpha$, which indicates that [there is an obvious the variation](#) trend

change in the sequence of time series is significant. Reverse the time series x to x_n, x_{n-1}, \dots, x_1 , and repeat the above process with $UB_k = -UF_k (k = n, n-1, \dots, 1)$.

Table 1. Definition of extreme temperature indices.

Index	Name	Definition	Category	Unit
SU	Summer days	Annual count of days when $T_{\max} > 25^{\circ}\text{C}$	Frequency	d
TX90p	Warm days	Annual count of days when $T_{\max} > 90^{\text{th}}$ percentile	Frequency	d
TXn	Minimum T_{\max}	Annual minimum value of T_{\max}	Intensity	$^{\circ}\text{C}$
TXs	Maximum T_{\max}	Annual maximum value of T_{\max}	Intensity	$^{\circ}\text{C}$
ID	Ice days	Annual count of days when $T_{\max} < 0^{\circ}\text{C}$	Frequency	d
TX10p	Cold days	Annual count of days when $T_{\max} < 10^{\text{th}}$ percentile	Frequency	d

4.5 Correlation analysis

Pearson correlation coefficient is often used to accurately measure the degree of correlation between two variables, and its size can reflect the strength of the correlation of the variables (Cao et al., 2020; Yan et al., 2021). For variables x_1, x_2, \dots, x_n and variables y_1, y_2, \dots, y_n , the correlation coefficient between them is calculated as Eq. (16).

$$R = \frac{n \sum_{i=1}^n (x_i \times y_i) - \sum_{i=1}^n x_i \sum_{i=1}^n y_i}{\sqrt{n \sum_{i=1}^n x_i^2 - (\sum_{i=1}^n x_i)^2} \sqrt{n \sum_{i=1}^n y_i^2 - (\sum_{i=1}^n y_i)^2}} \quad (16)$$

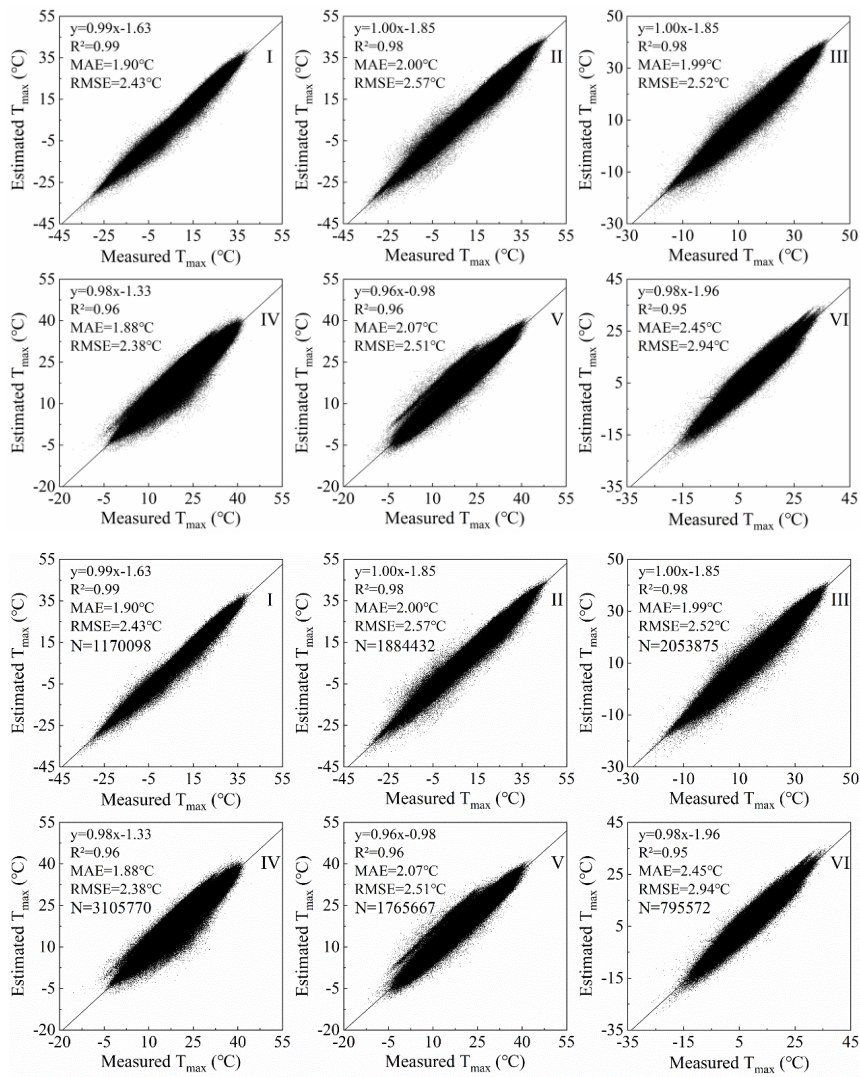
Here n is the total length of the time series. The value of the correlation coefficient R is between -1 and 1. $R < 0$ indicates a negative correlation. $R > 0$ indicates a positive correlation. The closer the absolute value of R is to 1, the closer the relationship between the two elements is.

5 Results

5.1 Validation

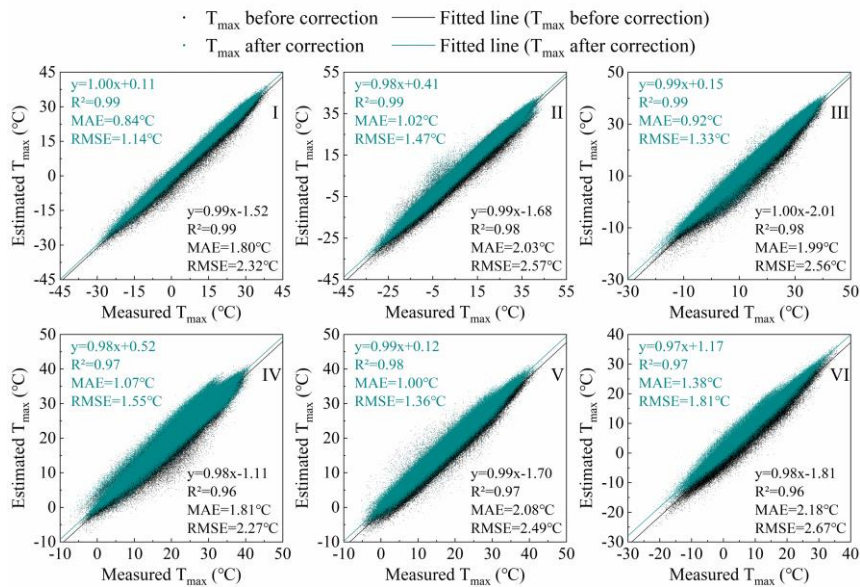
In order to verify the feasibility of T_{\max} estimation using the T_a diurnal variation model and to analyze the accuracy of T_{\max} estimation in different regions, scatter plots of estimated T_{\max} and measured T_{\max} in six natural regions (I, II, III, IV, V and VI) were drawn according to the regional division in Fig. 1. The results are shown in Fig. 4, and the validation in each region shows that the root mean square errors (RMSE) is between 2.38-2.94 $^{\circ}\text{C}$, and the mean absolute error (MAE) is

340 between 1.88-2.45°C, and the coefficient of determination (R^2) is between 0.95-0.99. [Among them In six regions,](#)
 341 the accuracy in region IV is the highest, while the accuracy is the lowest in region VI. As can be
 342 seen from Fig. 4, although most of the data is very accurate, some have some room for improvement.
 343 Therefore, further correction is needed to improve the accuracy of the T_{max} dataset.



344
345
346 **Figure 4.** Validation of T_{max} estimation results in each region.

347 The correction method in Sect. 4.1.2 was used to correct the T_{\max} estimation results of six regions
 348 separately. The comparison between T_{\max} before and after correction with the measured T_{\max} is
 349 shown in Fig. 5. It can be seen that T_{\max} corrected by the regression model is more consistent with
 350 the measured T_{\max} . The RMSE decreases from 2.38-2.94°C to 1.14-1.81°C, and the MAE decreases
 351 from 1.88-2.45°C to 0.84-1.38°C, and the R^2 increases from 0.96-0.99 to 0.97-0.99. The accuracy
 352 of T_{\max} is improved in each region after correction. The number of meteorological stations in region
 353 I is denser, and the accuracy of T_{\max} after calibration is significantly improved. The RMSE reduced
 354 from 2.32°C to 1.14°C, and the error is reduced by 51%. The number of meteorological stations in
 355 region VI is small, and the topography is undulating and the spatial heterogeneity is large. Therefore,
 356 the accuracy in this region is still the lowest among the six natural areas after correction. In general,
 357 the corrected T_{\max} dataset has higher consistency with the measured data, and which can be applied
 358 to research related to regional scale T_{\max} .



359

360 **Figure 5.** Validation of T_{\max} after correction.

361 5.2 Temporal and spatial changes of T_{\max}

362 5.2.1 Inter-annual variability

363 Fig. 6 shows the annual average change of T_{\max} in each region of China during 1979-2018. The T_{\max}
364 in each region exhibited an upward trend. However, due to the different geographical locations and
365 the influence of atmospheric circulation in various regions, the change of T_{\max} was also different.
366 The order of the T_{\max} increase in each region was: V>IV>III>Whole>VI>II>I. The T_{\max} anomaly
367 ranges of region I-VI and the whole China region were -1.41-1.53, -1.54-1.16, -1.47-1.12, -1.34-
368 0.92, -0.97-1.33, -1.31-1.15, and -1.09-0.98°C, respectively. The T_{\max} variation coefficients were
369 0.082, 0.045, 0.036, 0.024, 0.03, 0.088 and 0.038, respectively. It can be seen that T_{\max} fluctuated
370 the most in region VI and the least in region IV. The minimum values of region I-VI and China
371 region appeared in 1987, 1984, 1984, 1984, 1989, 1983, and 1984, respectively which were
372 distributed in the 1980s. The highest values of T_{\max} appeared in 2007, 2007, 2017, 2007, 2013, 1999,
373 and 2007 respectively. Zhai et al. (2016) found that 1999, 2007, and 2013 were among the 10 years
374 with the highest average T_a in China from 1900 to 2015. From 1998 to 2012, global surface
375 temperature experienced a warming hiatus (Du et al., 2019; Li et al., 2015), and T_{\max} in all regions
376 of China showed a downward trend during this period.

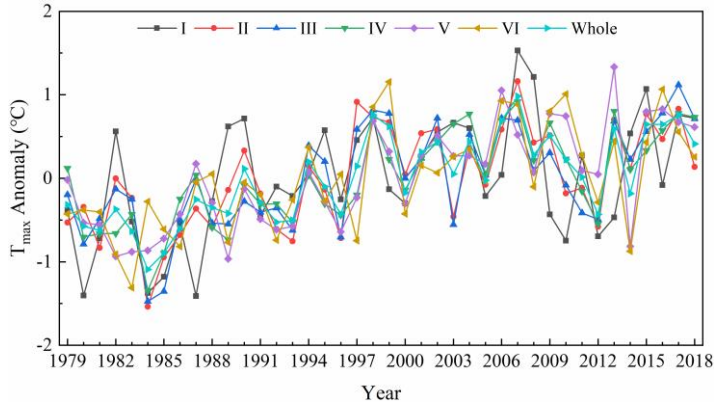


Figure 6. Inter-annual changes of T_{max} anomalies in six regions of China during 1979-2018.

377

378

379

380

381

382

383

384

385

386

387

388

389

390

391

In order to understand the spatial pattern and regional differences of T_{max} changes with more detail in China, Sen's slope estimation was used to calculate the annual average T_{max} change rate from 1979 to 2018 at the pixel scale (Fig. 7a). The significance test of the T_{max} change trend was conducted by the Mann-Kendall trend test (Fig. 7b). At the same time, the average change rate of T_{max} in each region and the area percentage of significant increase and decrease ($P < 0.05$) of T_{max} were calculated (Table 2). The results indicated that the annual average T_{max} change rate in most regions of China (78.24% of the study area) passed the significance test with a confidence of 0.05, and 65.84% of the pixels showed very significant changes in T_{max} ($P < 0.01$). Fig. 7a showed that the annual average T_{max} in most regions of China was on the rise, and the fastest rising rate of T_{max} was in western Yunnan. Only 8.13% of the regions in China showed a downward trend in T_{max} . These were concentrated mainly in the north and south of Xinjiang, and the northwest and south of Tibet. Among the six regions, the average T_{max} change rate of region V was the largest ($0.38^{\circ}\text{C}/10\text{a}$), and the average T_{max} change rate of region I and region II was the lowest ($0.31^{\circ}\text{C}/10\text{a}$) (Table 2).

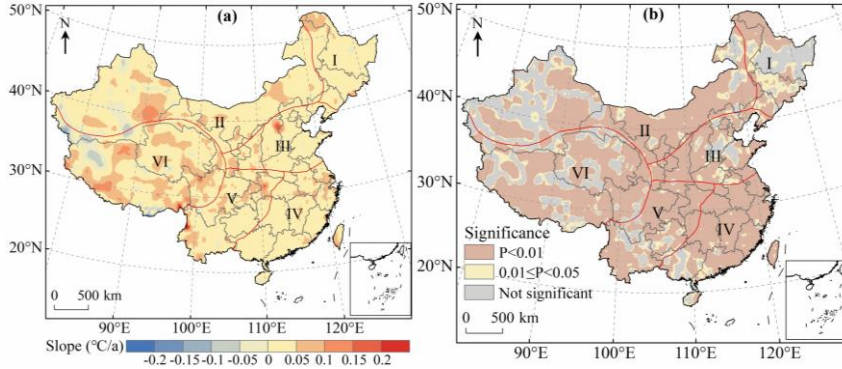


Figure 7. Inter-annual change rate of T_{max} (a) and results of Mann-Kendall trend test (b).

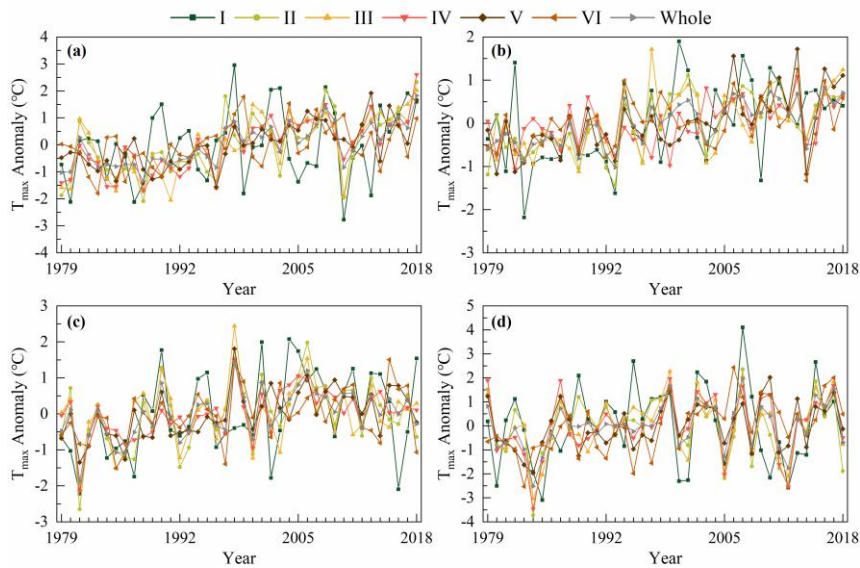
Table 2. Statistics of T_{max} change trends in various regions of China from 1979 to 2018.

Region	I	II	III	IV	V	VI	Whole
Mean ($^{\circ}\text{C}/10\text{a}$)	0.31	0.31	0.33	0.35	0.38	0.33	0.33
Significant upward (%)	65.21	69.45	87.03	92.29	87.00	67.93	75.13
Significant downward (%)	0.09	3.14	0	0.32	0.75	7.92	3.11

395 5.2.2 Seasonal changes

396 On the basis of the annual analysis, we also analyzed the seasonal changes. The seasons are divided
 397 according to the months (spring from March to May, summer from June to August, autumn from
 398 September to November, and winter from December to February). We plotted the seasonal variation
 399 curve of T_{max} in China from 1979 to 2018 (Fig. 8), and some information on the trend of T_{max}
 400 changes is shown in Table 3. The results indicated that T_{max} in each region fluctuated the most in
 401 winter and the least in summer. The highest T_{max} in each region in spring, summer, autumn and
 402 winter mostly occurred in 2018, 2013, 1998 and 2007, while the minimum T_{max} in each region in
 403 spring, summer, autumn and winter mostly occurred in 1988, 1993, 1981 and 1984. In 2013, T_{max}
 404 of region IV-VI in summer reached the highest since 1979, mainly due to the influence of the
 405 southwest monsoon, East Asian summer monsoon and other factors. Under the influence of El Niño,

406 T_{\max} in winter in region I, II and the whole study area was the highest in 2007. Under the influence
 407 of La Niña, the minimum T_{\max} in spring and winter in most areas of China appeared in 1988 and
 408 1984, respectively. In the same season, the variation trend of T_{\max} in each region was significantly
 409 different, and some even had opposing opposite trends. However, influenced by La Niña and the
 410 Eurasian atmospheric circulation, T_{\max} in winter in each region showed a consistent decreasing trend
 411 from 2007 to 2008. As can be seen from Table 3, in spring, summer, autumn and winter, the regions
 412 with the fastest T_{\max} rise in spring, summer, autumn and winter are III, I, I and VI respectively, and
 413 the regions with the lowest T_{\max} change rate are VI, VI, III and II respectively. We found that T_{\max}
 414 in winter of region II exhibited a very slight downward trend, but the sliding average of the 3-year
 415 and 5-year unit exhibited a weak upward trend.



416
 417 **Figure 8.** Changes of T_{\max} anomalies in various regions of China in spring (a), summer (b), autumn (c), winter (d)
 418 during 1979-2018.

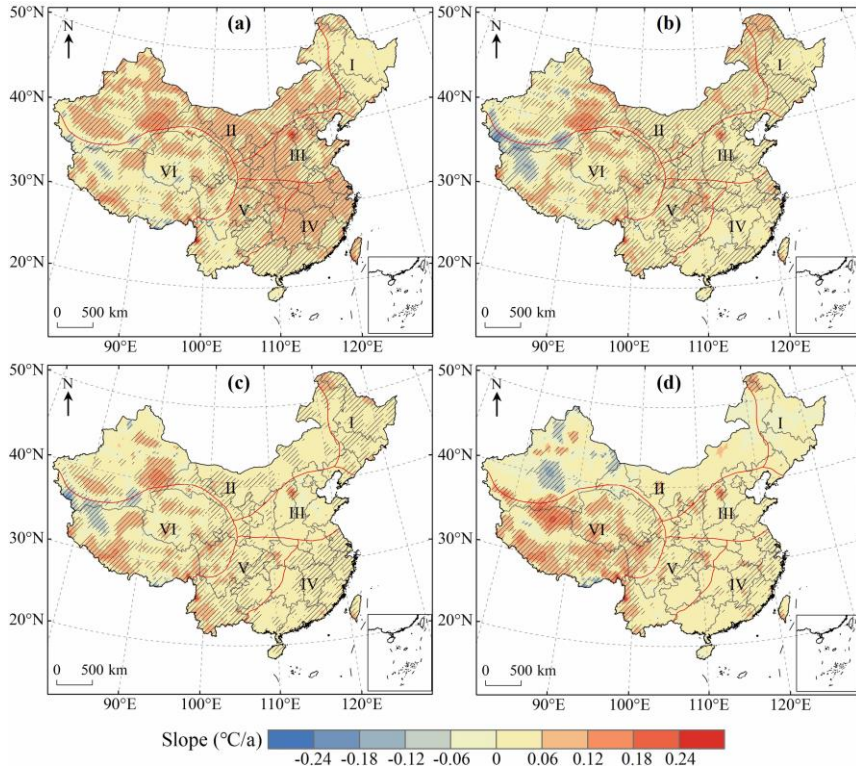
419 **Table 3.** Seasonal variation trend of T_{\max} in various regions of China from 1979 to 2018.

	I	II	III	IV	V	VI	Whole
--	---	----	-----	----	---	----	-------

Spring	0.035	0.063**	0.072**	0.063**	0.051**	0.026*	0.048**
Summer	0.040**	0.035**	0.033**	0.022**	0.039**	0.020*	0.031**
Autumn	0.039*	0.024	0.014	0.025**	0.035**	0.025*	0.023**
Winter	0.009	-0.002	0.027	0.037	0.034*	0.058**	0.027

420 (*, ** represent the trends are significant at the level of $p=0.05$, $p=0.01$, respectively.)

421 In order to display the seasonal variation characteristics of T_{max} in China more intuitively, we
422 drew the spatial distribution of the trend of T_{max} and conducted a significance test (Fig. 9).
423 Meanwhile, we counted the percentage of significant increase and decrease of T_{max} in each region
424 (Table 4). The results indicated that the areas with increasing T_{max} were more than those with
425 decreasing T_{max} in all seasons. From 1979 to 2018, the increasing trend of T_{max} was most significant
426 in spring, which accounted for 92.73% of the total study area, followed by autumn and summer,
427 while T_{max} increased the least in winter. Specifically, T_{max} increased significantly in most parts of
428 China in spring, and the region where T_{max} decreased significantly were mainly concentrated in the
429 region VI (Fig. 9a). In summer, T_{max} in most part of China showed a significant increasing trend,
430 but T_{max} in southern Xinjiang and northwestern Tibet exhibited a decreasing trend (Fig. 9b).
431 Compared with spring and summer, the area with a significant increasing trend of T_{max} in autumn
432 was smaller, and the regions with a significant decreasing trend of T_{max} were mainly distributed in
433 Xinjiang and Tibet (Fig. 9c). 79.02% of the regions experienced an increase in T_{max} in winter, which
434 was significantly lower than in other seasons. A significant increasing trend of T_{max} was observed
435 in the east of region IV, the southwest of regions V and VI, while the areas where T_{max} decreased
436 significantly were mainly observed in Xinjiang (Fig. 9d). We also observed no significant decrease
437 in T_{max} in regions I and III in spring, I in summer, I and IV in autumn, and III in winter (Table 4).
438 Further statistics showed that T_{max} of the whole region III showed an upward trend in spring.



439

440

Figure 9. Spatial distribution of the change trend of T_{max} in spring (a), summer (b), autumn (c), winter (d) over

441

China during 1979-2018. The shaded areas indicate trends that are significant at the 0.05 level.

442

Table 4. Change trend statistics of T_{max} in different seasons over China from 1979 to 2018.

	Significant upward (%)				Significant downward (%)			
	Spring	Summer	Autumn	Winter	Spring	Summer	Autumn	Winter
I	35.12	74.75	65.75	6.89	0	0	0	0.10
II	81.56	73.47	36.07	8.10	1.01	7.04	3.15	10.87
III	97.71	69.05	14.67	15.99	0	0.38	0.06	0
IV	96.20	46.80	57.26	29.47	0.35	0.68	0	0.44
V	76.48	75.11	58.56	31.62	1.24	1.53	0.06	0.12
VI	50.20	55.11	49.54	68.58	7.00	14.17	10.34	2.28
Whole	71.46	65.39	45.86	29.40	2.29	6.04	3.61	4.01

443

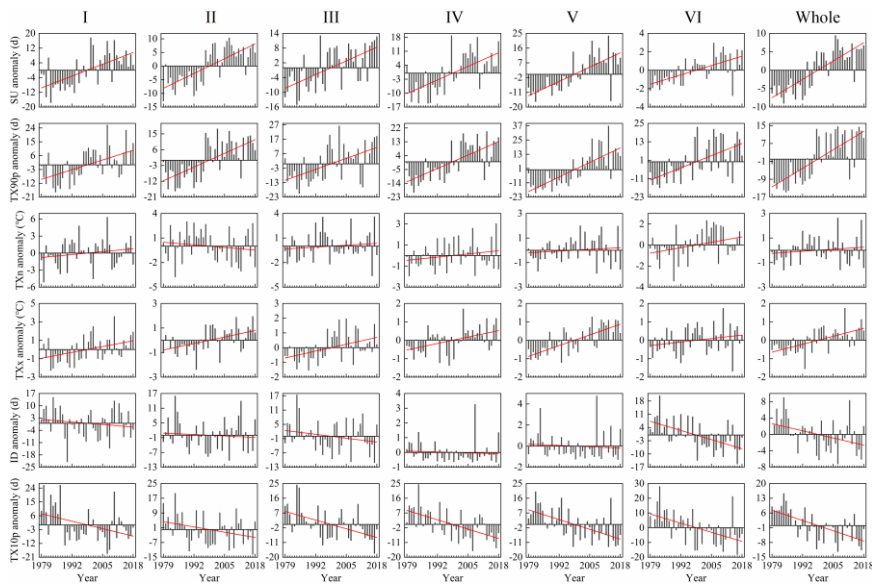
5.3 Temporal and spatial changes of extreme temperature indices

444

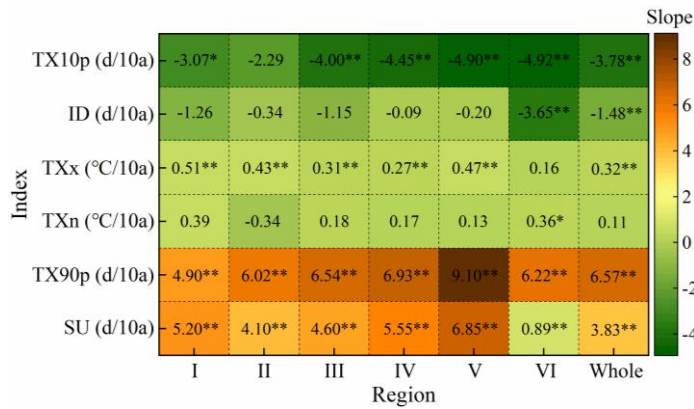
5.3.1 Change of time

445 We plotted the inter-annual variation of extreme temperature indices anomalies in various regions
446 of China from 1979 to 2018 (Fig. 10), and used Sen's slope estimation and the Mann-Kendall trend
447 test to calculate statistics on the trend of extreme temperature indices (Fig. 11). The results indicated
448 that SU, TX90p, TXn and TXx increased at a rate of 3.83d/10a, 6.57d/10a, 0.11°C/10a and
449 0.32°C/10a, respectively (Fig. 11). Influenced by the strong El Niño in 1997, the SU in all regions
450 exhibited a consistent upward trend from 1996 to 1997 (Fig. 10). The change rate of SU in all regions
451 passed the significance test of 0.01, indicating a significant upward trend (Fig. 11). The increasing
452 trend of TX90p in all regions was also very significant. The decadal average of TX90p in region
453 III-VI and the whole study area had an increasing trend, while the decadal average of TX90p in
454 region I and region II increased first and then decreased slightly. The TXn of region II showed a
455 weak decreasing trend, and the sliding average of the 3-year and 5-year periods also exhibited a
456 weak fluctuation downward trend. TXn of other regions showed an upward trend in general, and
457 only region VI had a significant increasing trend ($P < 0.05$) (Fig. 11). Except for region VI, the
458 change rate of TXx in other regions was higher than that of TXn. The rate of change of TXx
459 exhibited that the upward trend of region VI was not significant, while all other regions passed the
460 significance test of 0.01. During 1979-2018, ID and TX10p decreased significantly at the rate of -
461 1.48d/10a and -3.78d /10a, respectively ($P < 0.01$) (Fig. 11). The ID of all regions exhibited a
462 downward trend, with region VI and the whole study area showing the most obvious decline, passing
463 the significance test of 0.01 (Fig. 11). Compared with ID, TX10p decreased more sharply, and the
464 highest value of TX10p in all regions occurred before 1988 (Fig. 10). The above results indicate
465 that the frequency of high temperature events in China is on the rise, which is in line with the
466 expected results of global change. In addition, we also found that the occurrence time of maximum

467 and minimum values of SU, TXn, TXx and ID during 1979-2018 was consistent with previous
 468 research results (by Hong and Ying, (2018), which further proved the correctness of the T_{max}
 469 dataset constructed by us, indicating that built datathe dataset can be used to analyze the spatial-
 470 temporal changes of high temperature in China.



471
 472 **Figure 10.** Inter-annual trend of extreme temperature indices anomalies in different regions of China during 1979-
 473 2018.

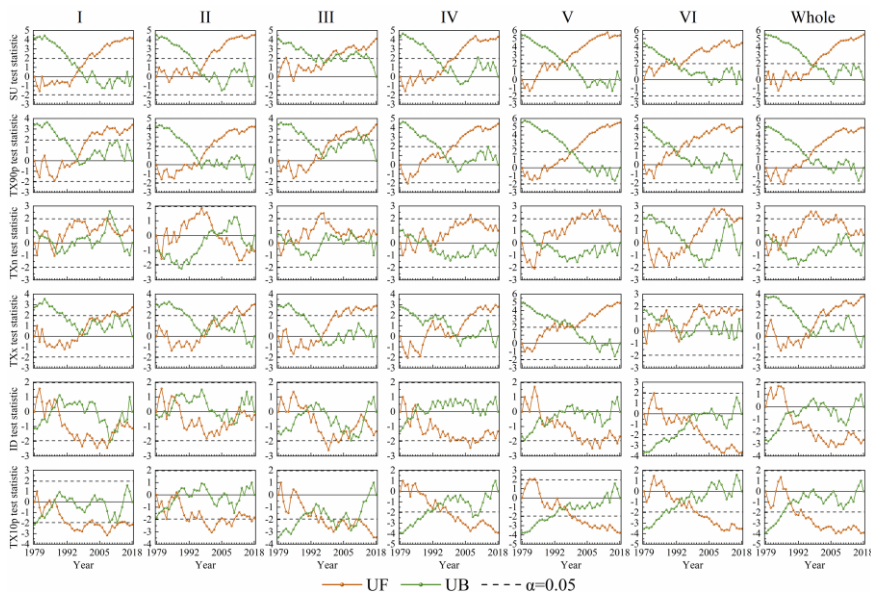


474

475 **Figure 11.** Variation trend of extreme temperature indices in different regions of China from 1979 to 2018. (*
476 significant at the 0.05 level, ** significant at the 0.01 level.)

477 In order to analyze the variation rules of extreme temperature indices in China from 1979 to
478 2018, the Mann-Kendall mutation test was applied to test the mutation characteristics of six extreme
479 temperature indices at the significance level of 0.05. The results are shown in Fig. 12. ~~During 1979-~~
480 ~~2018, We found that all the~~ extreme temperature indices had abrupt ~~changes~~change from 1979 to
481 2018, and 40% of the years where the abrupt changes occurred were El Niño years, while 46.7%
482 were La Niña years. ~~As can be seen from the intersection of the UF and UB curves, the SU of This~~
483 ~~finding further confirms that China is greatly affected by global climate change. TX90p in region~~
484 ~~III, V and VI had significant mutation in 2003, 1996 and 1990, respectively, while the other regions~~
485 ~~had no significant mutation in the whole I-II and the whole study area displayed an abrupt change~~
486 ~~from a period of 1979-2018. TX90p in each region exhibited an overall trend of decreasing first and~~
487 ~~then increasing. TX90p in region III was significantly mutated in 2011 and 2013, but the two~~
488 ~~mutations did not have much influence on the trend of TX90p. The TXn of region V showed a trend~~
489 ~~of first decreasing and then increasing, in contrast with the other regions, which all experienced a~~
490 ~~process of increasing and decreasing many times. lower value to one with higher value in 1996. After~~
491 ~~mutation in region II in 2003, TXn turned from an upward trend to a downward trend. Since the UF~~
492 ~~curve did not exceed the significance level, the, but the~~ downward trend was not obvious. The TXx
493 ~~of region V exhibited a decreasing trend from 1979 to 1984 but was not significant. After 1984, the~~
494 ~~TXx kept rising. The UF and UB curves intersected in 1999 and were outside the significance line~~
495 ~~at the level of 0.05, indicating that the TXx of region V had a significant mutation in 1999. The ID~~
496 ~~of the whole study area and its six sub-regions tended to increase first and then decrease, but the~~

497 upward trend was not significant. Except for region II, ID of other regions all showed a significant
 498 downward trend. There was a long period of decline in TX10p in all regions, and the UF value in
 499 region II was positive only in 1987. TX10p in region III-VI and the whole study area has been in a
 500 state of significant decline since 1996, 1997, 1998, 2000 and 1993, respectively.

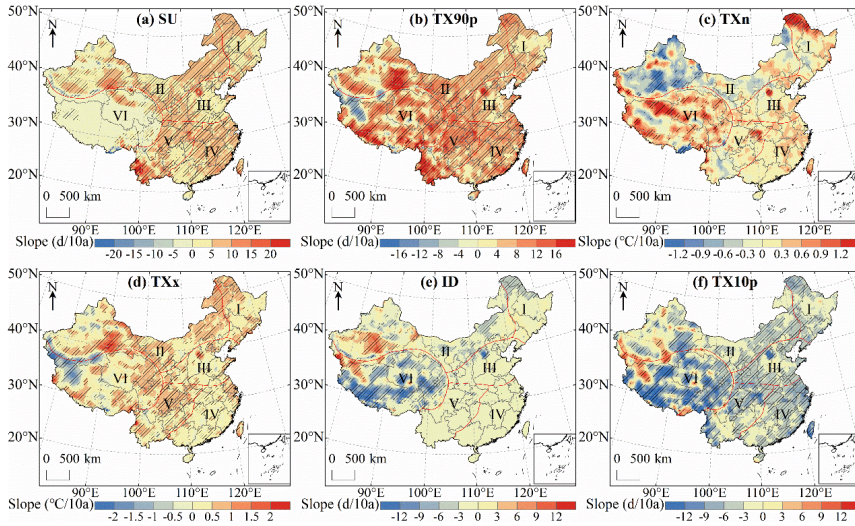


501
 502 **Figure 12.** MK abrupt change detection for the extreme temperature indices in different regions of China during
 503 1979-2018.

504 5.3.2 Spatial change

505 The spatial distribution of the extreme temperature indices trends in China during 1979-2018 is
 506 shown in Fig. 13 (a-f), while the area percentage of the increasing and decreasing trend of extreme
 507 temperature indices in each region is shown in Fig. 14 (a-f). For SU, TX90p, TXn and TXx, the area
 508 with rising trend is larger than the area with declining trend. The change of SU in most regions of
 509 China passed the significance test of 0.05, and the areas with significant increase accounted for 63.3%
 510 of the whole study area (Fig. 14a). The regions with no significant change in SU are were mainly

511 distributed in region VI (Fig. 13a). There ~~are~~were few days in a year when T_{\max} ~~exceeds~~exceeded
512 25°C in region VI, and T_{\max} in some regions ~~is~~was even lower than 25°C throughout the year, so the
513 change range of SU ~~is~~was small. The areas with a downward trend of TX90p were mainly distributed
514 in southern Xinjiang and northern Tibet (Fig. 13b). TX90p increased significantly in 75% of regions
515 in China ($P < 0.05$), and the area percentage of TX90p significantly increased in region V was the
516 largest among the six regions (Fig. 14b). The trend of TXn change in most regions of China was not
517 significant, and the significant decrease was mainly concentrated in region II and region VI (Fig.
518 13c). While other regions were dominated by increasing trend of the TXn, 69.7% of regions in
519 region II showed a downward trend (Fig. 14c). For TXx, its upward trend was slightly stronger than
520 TXn, and the region with the highest change rate was located in western China (Fig. 13d). The
521 regions with significantly decreased ID were mainly distributed in region VI (Fig. 13e). 75.7% of
522 the regions had a declining ID, and 53% of the regions passed the significance test (Fig. 14e). As
523 far as TX10p is concerned, its cooling trend was much stronger than that of ID, and the areas of
524 significant decline were widely distributed through all regions of China (Fig. 13f). The area with a
525 significant decrease in region IV accounted for 75.9% of the region, which was the largest among
526 the six regions (Fig. 14f).

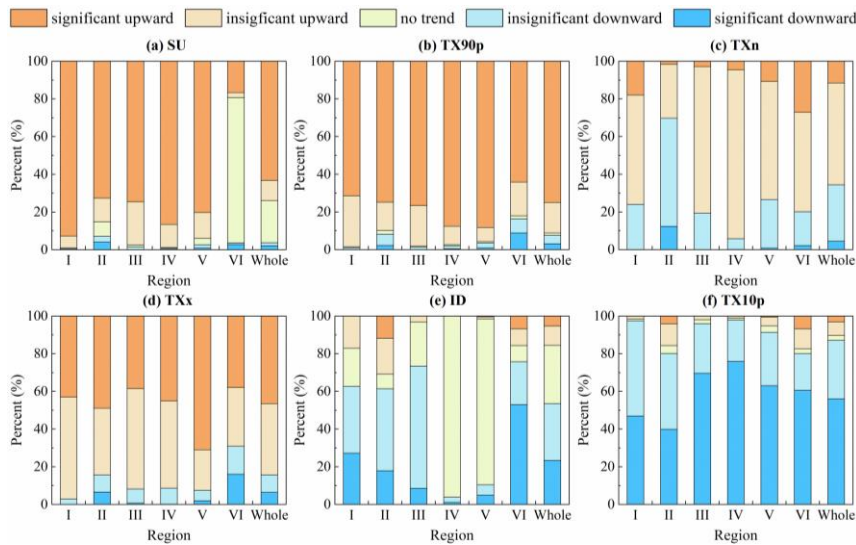


527

528 **Figure 13.** Spatial distribution of trends in extreme temperature indices over China during 1979-2018. The shaded

529

areas indicate trends that are significant at the 0.05 level.



530

531 **Figure 14.** Area percentage of the trend of extreme temperature indices in different regions of China during 1979-

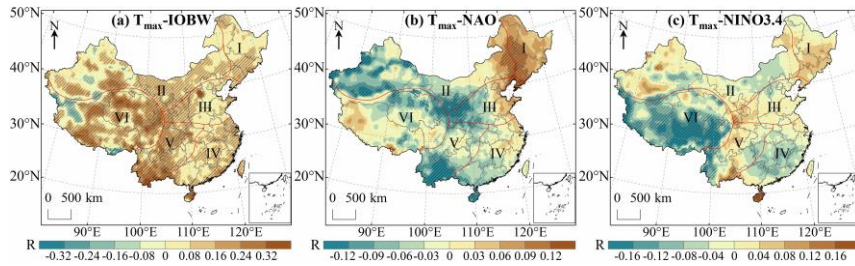
532

2018

533 **6 Discussion**

534 6.1 The influence of ocean climate modalities on T_{\max}

535 The correlation between T_{\max} anomalies and three climate modal indices in China during 1979-2018
536 is shown in Fig. 15 (a-c). The results show that there is a significant positive correlation between
537 T_{\max} and IOBW in 54.18% of the regions in China, which indicates that the warming of the Indian
538 Ocean will contribute to the warming trend of T_{\max} in these regions. T_{\max} had a moderate
539 positive correlation ($0.4 < R < 0.6$, $P < 0.01$) with IOBW in southern Yunnan and eastern Hainan
540 (Fig. 15a). T_{\max} and NAO had a significant positive correlation in northeast China, but the
541 (Fig. 15a). T_{\max} and NAO had a significant positive correlation in northeast China, but the
542 (Fig. 15a). T_{\max} and NAO had a significant positive correlation in northeast China, but the
543 had a significant positive correlation in northeast China, but the correlation was very weak ($R < 0.2$).
544 The percentage of T_{\max} anomaly value negatively correlated with NAO (16.55%) was higher than
545 that of NAO positively correlated (5.27%), mainly distributed in the west and south of region II,
546 west of region III, south of region IV and V, and northeast of region VI. This indicated that the
547 positive phase of NAO contribute to the decrease of T_{\max} in these regions (Fig. 15b). T_{\max} was
548 significantly positively correlated with NINO3.4 in southern China, central Xinjiang and southern
549 Gansu, indicating that El Niño events will lead to higher temperatures in these regions. In western
550 China and the middle part of region IV, T_{\max} was significantly negatively correlated with NINO3.4,
551 indicating that El Niño events will lead to cooling phenomena in these regions (Fig. 15c).

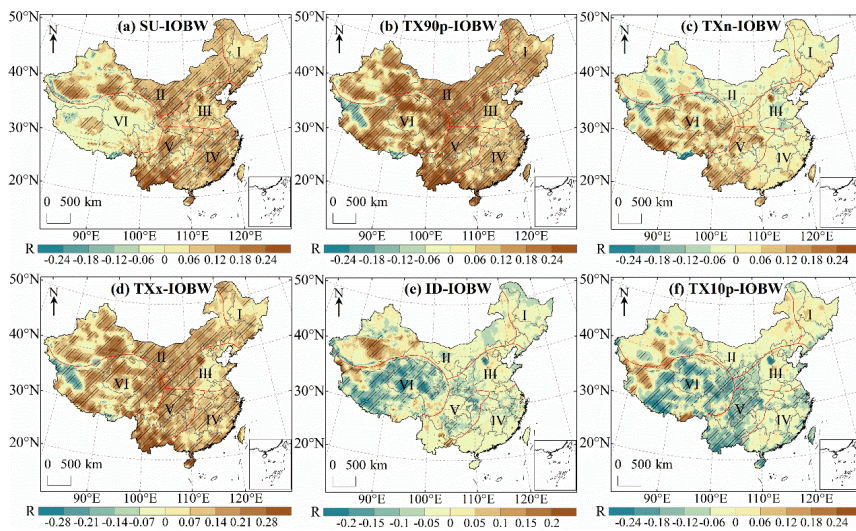


552
 553 **Figure 15.** Correlation analysis between T_{max} and IOBW (a), NAO (b) and NINO3.4 (c) in China during 1979-
 554 2018. The shaded areas indicate correlations that are significant at the 0.05 level.

555 **6.2 The influence of ocean climate mode on extreme temperature indices**

556 Fig. 16 (a-f) indicates the spatial distribution of the correlation between extreme temperature indices
 557 anomalies and IOBW in China during 1979-2018. It can be seen that SU, TX90p, TXn and TXx
 558 over most of China are positively correlated with the IOBW. The region with significant positive
 559 correlation between the SU and IOBW accounted for 42.67% of the whole study area, which
 560 indicated that a warming Indian Ocean would lead to the number of days over 25°C in these regions
 561 to increase. Significant negative correlations were found in northwest and southeast Tibet and the
 562 mountainous regions of southern Xinjiang (Fig. 16a). The area with the largest correlation
 563 coefficient is in the northeast of Hainan ($R=0.48$). The significant negative correlation between
 564 TX90p and IOBW was mainly distributed in region VI, but the negative correlation was not strong
 565 ($|R| < 0.4$) (Fig. 16b). The correlation coefficient between TXn and IOBW ranged from -0.34 to
 566 0.34, and the regions with significant positive correlation accounted for 16.65% of the whole study
 567 area. TXn and IOBW were significantly negatively correlated mainly in western China (Fig. 16c).
 568 Compared with TXn, the regions with significant correlation between TXx and IOBW were more
 569 widely distributed in China, among which the correlation coefficients in southern Yunnan and
 570 eastern Hainan were moderately positive ($0.4 < R < 0.6$) (Fig. 16d). ID and TX10p were negatively

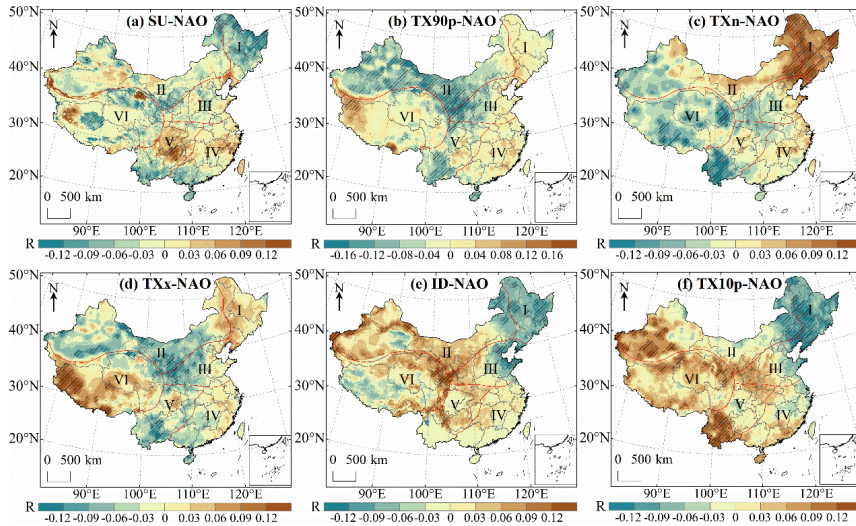
571 correlated with IOBW in most of China. The regions with significant negative correlation between
 572 ID and IOBW were mainly distributed in region VI, and the regions with significant positive
 573 correlation were mainly distributed in the west of region II (Fig. 16e). TX10p has a significant
 574 negative correlation with IOBW in more areas than ID, and the significant positive correlation was
 575 mainly located in western China (Fig. 16f).



576
 577 **Figure 16.** Correlation analysis between extreme temperature indices and IOBW in China during 1979-2018. The
 578 shaded areas indicate [correlations](#) that are significant at the 0.05 level.

579 The influence of NAO on the extreme temperature indices is shown in Fig.17 (a-f). SU, TX90p,
 580 TXx and TXn were negatively correlated with the NAO more than they were positively correlated
 581 with NAO, indicating that the positive phase of NAO would lead to the decline of SU, TX90p, TXx
 582 and TXn over most of China. SU and NAO had a significant positive correlation in southern
 583 Xinjiang, western Tibet, northern Qinghai and northern Guizhou, but the correlation was very weak
 584 ($R < 0.2$). There was no significant correlation between SU and NAO in southern Qinghai, which
 585 was consistent with previous observations (Ding et al., 2018). The region with the strongest negative

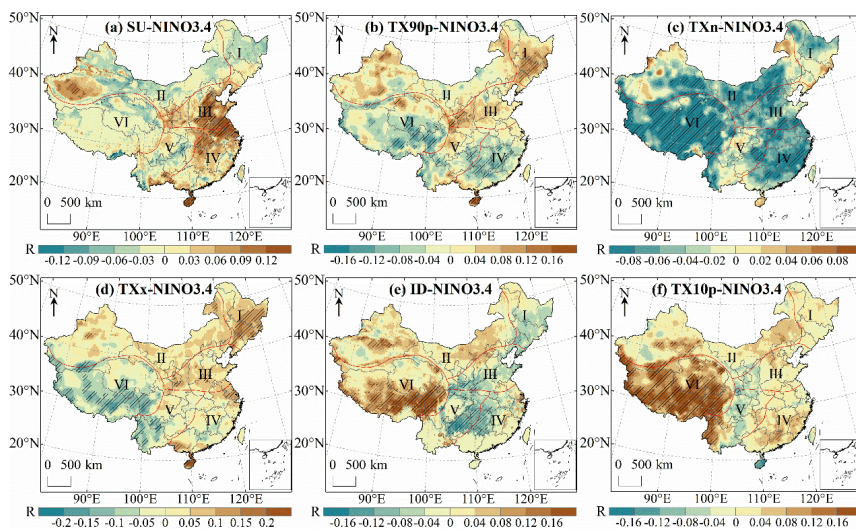
586 correlation between SU and NAO was located in Tibet ($R=-0.18$) (Fig. 17a). TX90p had a weak
587 negative correlation with NAO in eastern Xinjiang ($R=-0.22$, $P < 0.01$). TX90p was significantly
588 positively correlated with NAO in the west and south of region VI, but the correlation was extremely
589 weak (Fig. 17b). Shi et al. (2019) indicated that more regions had a significant positive correlation
590 between TXn and NAO in China than had a significant negative correlation, which was consistent
591 with our results. The areas of TXn had a significant positive correlation with NAO were mainly
592 distributed in northeast China, while the regions with significant negative correlation were mainly
593 located in central Tibet, eastern Qinghai and Yunnan (Fig. 17c). The correlation coefficient between
594 TXx and NAO varied from -0.16 to 0.21 . The regions with significant positive correlation between
595 TXx and NAO were mainly located in Tibet, and the region with the strongest correlation was
596 located in southern Tibet (Fig. 17d). The areas of ID was significantly positively correlated with
597 NAO accounted for 5.86% of the whole study area, and the strongest correlation was found in
598 western Xinjiang ($R=0.23$). The regions with significant negative correlation between ID and NAO
599 were mainly distributed in eastern and northeastern China (Fig. 17e). Sun et al. (2016) found a very
600 weak positive correlation between TX10p and NAO in the Loess Plateau, which was consistent with
601 our results. The regions with a significant negative correlation were mainly concentrated in
602 northeastern China (Fig. 17f).



603
 604 **Figure 17.** Correlation analysis between extreme temperature indices and NAO in China during 1979-2018. The
 605 shaded areas indicate correlations that are significant at the 0.05 level.

606 Fig.18 (a-f) shows the correlation between NINO3.4 and extreme temperature indices. The
 607 regions with significant positive correlation between SU and NINO3.4 were mainly distributed in
 608 eastern China, indicating that the events of El Niño would lead to an upward trend of SU in these
 609 regions. There were few regions with significant negative correlation between SU and NINO3.4,
 610 only accounting for 1.15% of the entire research area, mainly distributed in southeast Tibet and
 611 southwest Yunnan (Fig. 18a). The correlation coefficient between TX90p and NINO3.4 was -0.19-
 612 0.26. The areas of TX90p had a significant negative correlation with NINO3.4 were mainly
 613 distributed in region IV and VI (Fig. 18b). There was a significant negative correlation between
 614 TXn and NINO3.4 in 24.59% of regions, and the region with the strongest negative correlation was
 615 located in Tibet ($R=-0.25$). TXn was positively correlated with NINO3.4 in only 10.46% of regions
 616 in China, and the region with the largest correlation coefficient was northwest Xinjiang ($R=0.11$)
 617 (Fig. 18c). There was a weak positive correlation between TXx and NINO3.4 in southern

618 Guangdong and northern Hainan ($0.2 < R < 0.4$). The regions of TXx was significantly negatively
 619 correlated with NINO3.4 were mainly distributed in the south of region V and region VI (Fig. 18d).
 620 The significant negative correlation between ID and NINO3.4 was mainly concentrated in southern
 621 China. The areas with significant positive correlation were mainly distributed in the western region
 622 II and southern region VI, and the region with the strongest correlation was located in the western
 623 Sichuan ($R=0.31$) (Fig. 18e). TX10p in most regions of regional VI was significantly affected by
 624 NINO3.4, and the significant positive correlation area accounted for 69.31% of the whole region VI.
 625 TX10p was significantly negatively correlated with NINO3.4 in only 0.65% of regions in China,
 626 mainly distributed in Hainan and southern Gansu (Fig. 18f).



627
 628 **Figure 18.** Correlation analysis between extreme temperature indices and NINO3.4 in China during 1979-2018.

629 The shaded areas indicate [correlations](#) that are significant at the 0.05 level.

630 7 Conclusions

631 The global temperature continues to rise and extreme weather events continue to increase. [\(IPCC,](#)
 632 [2021\)](#). It is great significance to study regional high temperature changes. In order to obtain the key

633 parameters of high temperature spatial-temporal variation analysis, this study proposed a daily T_{\max}
634 estimation frame based on the near-surface T_a grid data and T_a diurnal variation model to build a
635 T_{\max} dataset in China from 1979 to 2018. Validation of T_{\max} estimation data in six natural regions
636 indicated that the RMSE of each region was between 2.38-2.94°C, the MAE was between 1.88-
637 2.45°C, and R^2 was between 0.95-0.99. After using the regression model to calibrate the dataset, the
638 accuracy of the estimated T_{\max} has been significantly improved. The RMSE of the T_{\max} after
639 calibration reduced to 1.14-1.81°C, and the MAE reduced to 0.84-1.38°C, and the R^2 increased to
640 0.97-0.99.

641 This dataset was used to study the spatial-temporal variation characteristics of T_{\max} and the
642 corresponding influencing factors in China, and to discuss the correlation between T_{\max} , extreme
643 temperature indices and ocean climate modal indices. T_{\max} in all regions of China exhibited an
644 upward trend from 1979 to 2018, with the largest rise in region V and the smallest rise in region I.
645 In spring, T_{\max} in China increased significantly in most regions, and the region III is with the fastest
646 rising speed. In winter, T_{\max} in China had the least significant rise, and the region II was with the
647 slowest rise rate. SU, TX90p and TXx in all regions showed an upward trend. Except for region II,
648 TXn in other regions also exhibited an upward trend, while ID and TX10p in all regions showed a
649 downward trend. All extreme temperature indices had abrupt changes during 1979-2018, and most
650 of the abrupt changes occurred in El Niño or La Niña years. The region with the largest increase of
651 SU, TX90p and TXx and the region with the largest decrease of TX10p were located in the western
652 Yunnan. The correlation analysis between T_{\max} and extreme temperature indices and ocean climate
653 modal indices indicated that the increase of the IOBW usually ~~led to~~ coincides with the increase of
654 T_{\max} , SU, TX90p, TXn and TXx and the decrease of ID and TX10p. NAO had the opposite

655 relationships. In most regions of China, T_{max} , SU, TX90p and TXn were negatively correlated with
656 NINO.3.4, while TXx, ID and TX10p were positively correlated with NINO.3.4._

657 The T_{max} dataset we produced can not only be used as the input parameters of climate change
658 models, crop growth models and carbon emission models, but also can be used to evaluate the risk
659 of high temperature disasters, which has high practical value. Currently, due to the limitation of the
660 temporal and spatial scope of the basic data, we have only produced the dataset of China. If global
661 station data and temperature data can be obtained in the future, we can continue to produce T_{max}
662 dataset on a global scale. The analysis of regional high temperature temporal and spatial changes
663 shows that the temperature changes in different regions of China are inconsistent, and the
664 mechanism that affects the temperature rise is different in different regions, and some regions are
665 highly correlated with ocean temperature changes. China is located in the eastern Eurasian continent
666 and the western Pacific Ocean. With the influence of the unique topography of the Qinghai-Tibet
667 Plateau, China's climate system is very complex. The temperature change in China is affected by a
668 combination of factors, and the ocean is only one of the factors affecting the temperature change in
669 China. Our study found that the influence of the ocean on China's temperature change is not
670 particularly strong, and we can continue to study the driving factors that have a strong impact on
671 China's climate change in the future. In order to strengthen environmental protection and control
672 temperature rise, and formulate reasonable carbon emission reduction measures, we need further
673 research in the future._

674

675 Code and Data availability. CMFD is available from the National Qinghai-Tibet Plateau Science
676 Data Center (<https://data.tpdc.ac.cn/>). ERA5 data can be obtained from the ECMWF ERA5 data

677 ~~website~~ Copernicus Climate Data Store (<https://cds.climate.copernicus.eu/>). Meteorological station
678 data is available by CMA National Meteorological Information Center (<http://data.cma.cn/>). IOBW
679 index can be accessed at the National Climate Center of CMA ([http://cmdp.ncc-
cma.net/cn/index.htm](http://cmdp.ncc-
680 cma.net/cn/index.htm)), and NAO index and NINO3.4 index are from the National Oceanic and
681 Atmospheric Administration of the United States (<https://psl.noaa.gov/data/climateindices/list/>).
682 The daily highest air temperature dataset and code can be downloaded at
683 <https://doi.org/10.5281/zenodo.6322881> (Wang et al., 2021).

684

685 *Author contributions.* PW and KM proposed the goals and aims of the research. FM provided
686 supervision and scientific guidance for the research. PW and SF built the dataset production model.
687 PW wrote the paper. KM, ZQ, SMB, and MA revised the final manuscript.

688

689 *Competing interests.* The authors declare no conflicts of interest.

690

691 *Acknowledgements.* The authors thank the China Meteorological Administration for providing
692 IOBW index and the ground measurements data, the Institute of Tibetan Plateau Research, Chinese
693 Academy of Sciences for providing CMFD dataset, and the NASA Earth Observing System Data
694 and Information System for providing the DEM data. We also thank the National Oceanic and
695 Atmospheric Administration of the United States for providing the ocean climate modal indices and
696 the ECMWF for providing the climate reanalysis data.

697

698 *Financial support.* This work is supported by the Framework Project of APSCO Member States
699 (Global and key regional drought forecasting and monitoring) & National Key Research and

700 Development Program of China (2019YFE0127600), the Fundamental Research Funds for Central
701 Nonprofit Scientific Institution (1610132020014) and the Open Fund of the State Key Laboratory
702 of Remote Sensing Science.

703

704 References

- 705 Abdullah, A. M., Ismail, M., Yuen, F. S., Abdullah, S., and Elhadi, R. E.: The Relationship between
706 Daily Maximum Temperature and Daily Maximum Ground Level Ozone Concentration, Polish
707 Journal of Environmental Studies, 26, 517-523, <https://doi.org/10.15244/pjoes/65366>, 2017.
- 708 Basu, R.: High ambient temperature and mortality: a review of epidemiologic studies from 2001 to 2008,
709 Environmental health, 8, 40, <https://doi.org/10.1186/1476-069X-8-40>, 2009.
- 710 Benali, A., Carvalho, A. C., Nunes, J. P., Carvalhais, N., and Santos, A.: Estimating air surface
711 temperature in Portugal using MODIS LST data, Remote Sensing of Environment, 124, 108-121,
712 <https://doi.org/10.1016/j.rse.2012.04.024>, 2012.
- 713 Ding, Z. Y., Wang, Y. Y., and Lu, R. J.: An analysis of changes in temperature extremes in the Three
714 River Headwaters region of the Tibetan Plateau during 1961-2016, Atmospheric Research, 209, 103-
715 114, <https://doi.org/10.1016/j.atmosres.2018.04.003>, 2018.
- 716 Ding, Z. Y., Wang, Y. Y., and Lu, R. J.: An analysis of changes in temperature extremes in the Three
717 River Headwaters region of the Tibetan Plateau during 1961-2016, Atmospheric Research, 209, 103-
718 114, <https://doi.org/10.1016/j.atmosres.2018.04.003>, 2018.
- 719 Du, Q. Q., Zhang, M. J., Wang, S. J., Che, C. W., Ma, R., and Ma, Z. Z.: Changes in air temperature over
720 China in response to the recent global warming hiatus, Journal of Geographical Sciences, 29, 496-516,
721 <https://doi.org/10.1007/s11442-019-1612-3>, 2019.
- 722 Ephraïm, J. E., Goudriaan, J., and Marani, A.: Modelling diurnal patterns of air temperature, radiation
723 wind speed and relative humidity by equations from daily characteristics, Agricultural Systems, 51,
724 377-393, [https://doi.org/10.1016/0308-521X\(95\)00068-G](https://doi.org/10.1016/0308-521X(95)00068-G), 1996.
- 725 Evrendilek, F., Karakaya, N., Gungor, K., and Aslan, G.: Satellite-based and mesoscale regression
726 modeling of monthly air and soil temperatures over complex terrain in Turkey, Expert Systems with
727 Applications, 39, 2059-2066, <https://doi.org/10.1016/j.eswa.2011.08.023>, 2012.
- 728 Fabiola, F. P. and Mario, L. S.: Simple air temperature estimation method from MODIS satellite images
729 on a regional scale, Chilean Journal of Agricultural Research, 70, 436-445,
730 <https://doi.org/10.4067/S0718-58392010000300011>, 2010.
- 731 Gasparrini, A. and Armstrong, B.: The impact of heat waves on mortality, Epidemiology, 22, 68-73,
732 <https://doi.org/10.1097/EDE.0b013e3181fdcd99>, 2011.
- 733 Gu, H. H., Yu, Z. B., Peltier, W. R., and Wang, X. Y.: Sensitivity studies and comprehensive evaluation
734 of RegCM4. 6.1 high-resolution climate simulations over the Tibetan Plateau, Climate Dynamics, 54,
735 3781-3801, <https://doi.org/10.1007/s00382-020-05205-6>, 2020.
- 736 Guan, Y. H., Zhang, X. C., Zheng, F. L., and Wang, B.: Trends and variability of daily temperature
737 extremes during 1960–2012 in the Yangtze River Basin, China, Global and Planetary Change, 124,
738 79-94, <https://doi.org/10.1016/j.gloplacha.2014.11.008>, 2015.

739 He, J., Yang, K., Tang, W. J., Lu, H., Qin, J., Chen, Y. Y., and Li, X.: The first high-resolution
740 meteorological forcing dataset for land process studies over China, *Scientific Data* 7, 1-11,
741 <https://doi.org/10.1038/s41597-020-0369-y>, 2020.

742 [Hersbach, H., Bell, B., Berrisford, P., Hirahara, S., Horónvi, A., Muñoz - Sabater, J., Nicolas, J., Peubey,](#)
743 [C., Radu, R., Schepers, D., Simmon, A., Soci, C., Abdalla, S., Abellan, X., Balsamo, G., Bechtold, P.,](#)
744 [Biavati, G., Bidlot, J., Bonavita, M., De Chiara, G., Dahlgren, P., Dee, D., Diamantakis, M., Dragani,](#)
745 [R., Flemming, J., Forbes, R., Fuentes, M., Geer, A., Haimberger, L., Healy, S., Hogan, R. J., Hólm,](#)
746 [E., Janisková, M., Keeley, S., Laloyaux, P., Lopez, P., Lupu, C., Radnoti, G., de Rosnay, P., Rozum,](#)
747 [I., Vamborg, F., Villaume, S., and Thépaut, J.-N.: The ERA5 global reanalysis, *Quarterly Journal of*](#)
748 [the Royal Meteorological Society, 146, 1999-2049, <https://doi.org/10.1002/qj.3803>, 2020.](#)

749 Hoffmann, L., Günther, G., Li, D., Stein, O., Wu, X., Griessbach, S., Heng, Y., Konopka, P., Müller, R.,
750 Vogel, B., and Wright, J. S.: From ERA-Interim to ERA5: the considerable impact of ECMWF's next-
751 generation reanalysis on Lagrangian transport simulations, *Atmospheric Chemistry and Physics*, 19,
752 3097-3124, <https://doi.org/10.5194/acp-19-3097-2019>, 2019.

753 Hong, Y. and Ying, S.: Characteristics of extreme temperature and precipitation in China in 2017 based
754 on ETCCDI indices, *Advances in Climate Change Research*, 9, 218-226,
755 <https://doi.org/10.1016/j.accre.2019.01.001>, 2018.

756 [IPCC: Weather and Climate Extreme Events in a Changing Climate, Cambridge University Press,](#)
757 [Cambridge, <https://doi.org/10.1017/9781009157896.013>, 2021.](#)

758 Johnson, M. E. and Fitzpatrick, E. A.: A comparison of two methods of estimating a mean diurnal
759 temperature curve during the daylight hours, *Archiv für Meteorologie, Geophysik und*
760 *Bioklimatologie, Serie B*, 25, 251-263, <https://doi.org/10.1007/BF02243056>, 1977.

761 Khan, N., Shahid, S., Ismail, T. B., and Wang, X. J.: Spatial distribution of unidirectional trends in
762 temperature and temperature extremes in Pakistan, *Theoretical and Applied Climatology*, 136, 899-
763 913, <https://doi.org/10.1007/s00704-018-2520-7>, 2018.

764 Kleinert, F., Leufen, L. H., and Schultz, M. G.: IntelliO3-ts v1. 0: a neural network approach to predict
765 near-surface ozone concentrations in Germany, *Geoscientific Model Development*, 14, 1-25,
766 <https://doi.org/10.5194/gmd-14-1-2021>, 2021.

767 Li, L. C., Yao, N., Li, Y., Liu, D. L., Wang, B., and Ayantobo, O. O.: Future projections of extreme
768 temperature events in different sub-regions of China, *Atmospheric Research*, 217, 150-164,
769 <https://doi.org/10.1016/j.atmosres.2018.10.019>, 2019a.

770 Li, Q. X., Yang, S., Xu, W. H., Wang, X. L., Jones, P., Parker, D., Zhou, L. M., Feng, Y., and Gao, Y.:
771 China experiencing the recent warming hiatus, *Geophysical Research Letters*, 42, 889-898,
772 <https://doi.org/10.1002/2014GL062773>, 2015.

773 Li, Y. L., Han, W. Q., Zhang, L., and Wang, F.: Decadal SST variability in the southeast Indian Ocean
774 and its impact on regional climate, *Journal of Climate*, 32, 6299-6318, <https://doi.org/10.1175/JCLI->
775 [D-19-0180.1](#), 2019b.

776 Lin, S. P., Moore, N. J., Messina, J. P., DeVisser, M. H., and Wu, J. P.: Evaluation of estimating daily
777 maximum and minimum air temperature with MODIS data in east Africa, *International Journal of*
778 *Applied Earth Observation and Geoinformation*, 18, 128-140,
779 <https://doi.org/10.1016/j.jag.2012.01.004>, 2012.

780 Luan, J. K., Zhang, Y. Q., Tian, J., Meresa, H. K., and Liu, D. F.: Coal mining impacts on catchment
781 runoff, *Journal of Hydrology*, 589, 125101, <https://doi.org/10.1016/j.jhydrol.2020.125101>, 2020.

782 McGree, S., Herold, N., Alexander, L., Schreider, S., Kuleshov, Y., Ene, E., Finaulahi, S., Inape, K.,
783 Mackenzie, B., Malala, H., Ngari, A., Prakash, B., and Tahani, L.: Recent changes in mean and
784 extreme temperature and precipitation in the Western Pacific Islands, *Journal of Climate*, 32, 4919-
785 4941, <https://doi.org/10.1175/JCLI-D-18-0748.1> 2019.

786 Ninyerola, M., Pons, X., and Roure, J. M.: A methodological approach of climatological modelling of
787 air temperature and precipitation through GIS techniques, *International Journal of Climatology*, 20,
788 1823-1841, [https://doi.org/10.1002/1097-0088\(20001130\)20:14<1823::AID-JOC566>3.0.CO;2-B](https://doi.org/10.1002/1097-0088(20001130)20:14<1823::AID-JOC566>3.0.CO;2-B),
789 2000.

790 Parton, W. J. and Logan, J. A.: A model for diurnal variation in soil and air temperature, *Agricultural*
791 *Meteorology*, 23, 205-216, [https://doi.org/10.1016/0002-1571\(81\)90105-9](https://doi.org/10.1016/0002-1571(81)90105-9), 1981.

792 Poudel, A., Cuo, L., Ding, J., and Gyawali, A. R.: Spatio - temporal variability of the annual and monthly
793 extreme temperature indices in Nepal, *International Journal of Climatology*, 40, 4956-4977,
794 <https://doi.org/10.1002/joc.6499>, 2020.

795 Ruml, M., Gregorić, E., Vujadinović, M., Radovanović, S., Matović, G., Vuković, A., Počuča, V., and
796 Stojičić, D.: Observed changes of temperature extremes in Serbia over the period 1961 – 2010,
797 *Atmospheric Research*, 183, 26-41, <https://doi.org/10.1016/j.atmosres.2016.08.013>, 2017.

798 Salman, S. A., Shahid, S., Ismail, T., Chung, E.-S., and Al-Abadi, A. M.: Long-term trends in daily
799 temperature extremes in Iraq, *Atmospheric Research*, 198, 97-107,
800 <https://doi.org/10.1016/j.atmosres.2017.08.011>, 2017.

801 Sathaye, J. A., Dale, L. L., Larsen, P. H., Fitts, G. A., Koy, K., Lewis, S. M., and de Lucena, A. F. P.:
802 Estimating impacts of warming temperatures on California's electricity system, *Global Environmental*
803 *Change*, 23, 499-511, <https://doi.org/10.1016/j.gloenvcha.2012.12.005>, 2013.

804 Seenu, P. Z. and Jayakumar, K. V.: Comparative study of innovative trend analysis technique with Mann-
805 Kendall tests for extreme rainfall, *Arabian Journal of Geosciences*, 14, 1-15,
806 <https://doi.org/10.1007/s12517-021-06906-w>, 2021.

807 Sehra, S. T., Salciccioli, J. D., Wiebe, D. J., Fundin, S., and Baker, J. F.: Maximum daily temperature,
808 precipitation, ultraviolet light, and rates of transmission of severe acute respiratory syndrome
809 coronavirus 2 in the United States, *Clinical Infectious Diseases*, 71, 2482-2487,
810 <https://doi.org/10.1093/cid/ciaa681>, 2020.

811 Sen, P. K.: Estimates of the regression coefficient based on Kendall's tau, *Journal of the American*
812 *Statistical Association*, 63, 1379-1389, <https://doi.org/10.2307/2285891> 1968.

813 Shen, S. H. and Leptoukh, G. G.: Estimation of surface air temperature over central and eastern Eurasia
814 from MODIS land surface temperature, *Environmental Research Letters*, 6, 045206,
815 <https://doi.org/10.1088/1748-9326/6/4/045206> 2011.

816 Shi, J., Cui, L. L., Wang, J. B., Du, H. Q., and Wen, K. M.: Changes in the temperature and precipitation
817 extremes in China during 1961–2015, *Quaternary International*, 527, 64-78,
818 <https://doi.org/10.1016/j.quaint.2018.08.008>, 2019.

819 Sun, W. Y., Mu, X. M., Song, X. Y., Wu, D., Cheng, A. F., and Qiu, B.: Changes in extreme temperature
820 and precipitation events in the Loess Plateau (China) during 1960–2013 under global warming,
821 *Atmospheric Research*, 168, 33-48, <http://dx.doi.org/10.1016/j.atmosres.2015.09.001>, 2016.

822 Sun, Y. J., Wang, J. F., Zhang, R. H., Gillies, R. R., Xue, Y., and Bo, Y. C.: Air temperature retrieval
823 from remote sensing data based on thermodynamics, *Theoretical and Applied Climatology*, 80, 37-48,
824 <https://doi.org/10.1007/s00704-004-0079-y>, 2005.

825 Tan, M. L., Samat, N., Chan, N. W., Lee, A. J., and Li, C.: Analysis of Precipitation and Temperature
826 Extremes over the Muda River Basin, Malaysia, *Water*, 11, 1-16, <https://doi.org/10.3390/w11020283>,
827 2019.

828 Tong, S. Q., Li, X. Q., Zhang, J. Q., Bao, Y. H., Bao, Y. B., Na, L., and Si, A. L.: Spatial and temporal
829 variability in extreme temperature and precipitation events in Inner Mongolia (China) during 1960–
830 2017, *Science of the Total Environment*, 649, 75-89, <https://doi.org/10.1016/j.scitotenv.2018.08.262>,
831 2019.

832 Urraca, R., Huld, T., Gracia-Amillo, A., Martinez-de-Pison, F. J., Kaspar, F., and Sanz-Garcia, A.:
833 Evaluation of global horizontal irradiance estimates from ERA5 and COSMO-REA6 reanalyses using
834 ground and satellite-based data, *Solar Energy*, 164, 339-354,
835 <https://doi.org/10.1016/j.solener.2018.02.059>, 2018.

836 Wang, X. X., Jiang, D. B., and Lang, X. M.: Extreme temperature and precipitation changes associated
837 with four degree of global warming above pre - industrial levels, *International Journal of Climatology*,
838 39, 1822-1838, <https://doi.org/10.1002/joc.5918>, 2019.

839 Wang, Y., Peng, D. L., Shen, M. G., Xu, X. Y., Yang, X. H., Huang, W. J., Yu, L., Liu, L. Y., Li, C. J.,
840 and Li, X. W.: Contrasting Effects of Temperature and Precipitation on Vegetation Greenness along
841 Elevation Gradients of the Tibetan Plateau, *Remote Sensing*, 12, 2751,
842 <https://doi.org/10.3390/rs12172751>, 2020.

843 Wloczyk, C., Borg, E., Richter, R., and Miegel, K.: Estimation of instantaneous air temperature above
844 vegetation and soil surfaces from Landsat 7 ETM+ data in northern Germany, *International Journal of*
845 *Remote Sensing*, 32, 9119-9136, <https://doi.org/10.1080/01431161.2010.550332>, 2011.

846 Wu, R. G., Yang, S., Liu, S., Sun, L., Lian, Y., and Gao, Z. T.: Northeast China summer temperature and
847 north Atlantic SST, *Journal of Geophysical Research*, 116, <https://doi.org/10.1029/2011JD015779>,
848 2011.

849 Yang, Z. Y., Shen, M. G., Jia, S. G., Guo, L., Yang, W., Wang, C., Chen, X. H., and Chen, J.: Asymmetric
850 responses of the end of growing season to daily maximum and minimum temperatures on the Tibetan
851 Plateau, *Journal of Geophysical Research*, 122, 278-287, <https://doi.org/10.1002/2017JD027318>,
852 2017.

853 Yang, Z. Y., Shen, M. G., Jia, S. G., Guo, L., Yang, W., Wang, C., Chen, X. H., and Chen, J.: Asymmetric
854 responses of the end of growing season to daily maximum and minimum temperatures on the Tibetan
855 Plateau, *Journal of Geophysical Research*, 122, 278-287, <https://doi.org/10.1002/2017JD027318>,
856 2017.

857 Yoo, C., Im, J., Park, S., and Quackenbush, L. J.: Estimation of daily maximum and minimum air
858 temperatures in urban landscapes using MODIS time series satellite data, *ISPRS Journal of*
859 *Photogrammetry and Remote Sensing*, 137, 149-162, <https://doi.org/10.1016/j.isprsjprs.2018.01.018>,
860 2018.

861 You, Q. L., Kang, S. C., Aguilar, E., Pepin, N., Flügel, W.-A., Yan, Y. P., Xu, Y. W., Zhang, Y. J., and
862 Huang, J.: Changes in daily climate extremes in China and their connection to the large scale
863 atmospheric circulation during 1961–2003, *Climate Dynamics*, 36, 2399-2417,
864 <https://doi.org/10.1007/s00382-009-0735-0>, 2011.

865 Zhai, P. M., Yu, R., Guo, Y. J., Li, Q. X., Ren, X. J., Wang, Y. Q., Xu, W. H., Liu, Y. J., and Ding, Y.
866 H.: The strong El Niño in 2015/2016 and its dominant impacts on global and China's climate, *Acta*
867 *Meteorologica Sinica*, 74, 309-321. (In Chinese), <https://doi.org/10.11676/qxb2016.049>, 2016.

868 Zhang, H., Da, Y. B., Zhang, X., and Fan, J. L.: The impacts of climate change on coal-fired power plants:
869 evidence from China, *Energy & Environmental Science*, 14, 4890-4902,
870 <https://doi.org/10.1039/D1EE01475G>, 2021.

871 Zhang, M., Du, S. Q., Wu, Y. J., Wen, J. H., Wang, C. X., Xu, M., and Wu, S. Y.: Spatiotemporal changes
872 in frequency and intensity of high-temperature events in China during 1961-2014, *Journal of*
873 *Geographical Sciences*, 27, 1027-1043, <https://doi.org/10.1007/s11442-017-1419-z>, 2017.

874 Zhang, P. F., Ren, G. Y., Xu, Y., Wang, X. L. L., Qin, Y., Sun, X. B., and Ren, Y. Y.: Observed changes
875 in extreme temperature over the global land based on a newly developed station daily dataset, *Journal*
876 *of Climate*, 32, 8489-8509, <https://doi.org/10.1175/JCLI-D-18-0733.1> 2019.

877 Zhao, B., Mao, K. B., Cai, Y. L., Shi, J. C., Li, Z. L., Qin, Z. H., Meng, X. J., Shen, X. Y., and Guo, Z.
878 H.: A combined Terra and Aqua MODIS land surface temperature and meteorological station data
879 product for China from 2003 to 2017, *Earth System Science Data*, 12, 2555-2577,
880 <https://doi.org/10.5194/essd-12-2555-2020>, 2020.

881 Zheng, X., Zhu, J. J., and Yan, Q. L.: Monthly air temperatures over Northern China estimated by
882 integrating MODIS data with GIS techniques, *Journal of Applied Meteorology and Climatology*, 52,
883 1987-2000, <https://doi.org/10.1175/JAMC-D-12-0264.1> 2013.

884 Zhong, K. Y., Zheng, F. L., Wu, H. Y., Qin, C., and Xu, X. M.: Dynamic changes in temperature extremes
885 and their association with atmospheric circulation patterns in the Songhua River Basin, China,
886 *Atmospheric Research*, 190, 77-88, <https://doi.org/10.1016/j.atmosres.2017.02.012>, 2017.

887 Zhou, B. T., Xu, Y., Wu, J., Dong, S. Y., and Shi, Y.: Changes in temperature and precipitation extreme
888 indices over China: Analysis of a high - resolution grid dataset, *International Journal of Climatology*,
889 36, 1051-1066, <https://doi.org/10.1002/joc.4400>, 2016.

890 Zhu, S. Y., Zhou, C. X., Zhang, G. X., Zhang, H. L., and Hua, J. W.: Preliminary verification of
891 instantaneous air temperature estimation for clear sky conditions based on SEBAL, *Meteorology and*
892 *Atmospheric Physics*, 129, 71-81, <https://doi.org/10.1007/s00703-016-0451-3>, 2017.

893 Zhu, W. B., Lü, A. F., and Jia, S. F.: Estimation of daily maximum and minimum air temperature using
894 MODIS land surface temperature products, *Remote Sensing of Environment*, 130, 62-73,
895 <http://dx.doi.org/10.1016/j.rse.2012.10.034>, 2013.

896